A framework based on 2-D Taylor expansion for quantifying the impacts of sub-pixel reflectance variance and covariance on cloud optical thickness and effective radius retrievals based on the bi-spectral method

Z. Zhang[1,2,*], F. Werner[2], H.-M. Cho[2,3], G. Wind,[4,5]
S. Platnick[4], A. S. Ackerman[6], L. Di Girolamo[7], and A. Marshak[4], Kerry Meyer[4,8]

1. Physics Department, UMBC, Baltimore, MD, USA
2. Joint Center for Earth Systems Technology, UMBC, Baltimore, MD, USA
3. Electronics and Telecommunications Research Institute, Korea
4. NASA Goddard Space Flight Center, Greenbelt, MD, USA
5. Science Systems and Applications, Inc., Maryland 20706, USA
6. NASA Goddard Institute for Space Studies, New York City, NY, USA
7. Department of Atmospheric Sciences, University of Illinois, Urbana-Champaign, IL, USA
8. Universities Space Research Association (USRA), Columbia, MD, USA

For Publication in JGR-Atmosphere

*Corresponding author: Zhibo Zhang
Email: Zhibo.Zhang@umbc.edu

Abstract:

The bi-spectral method retrieves cloud optical thickness (τ) and cloud droplet effective radius (r_e) simultaneously from a pair of cloud reflectance observations, one in a visible or near infrared (VIS/NIR) band and the other in a shortwave-infrared (SWIR) band. A cloudy pixel is usually assumed to be horizontally homogeneous in the retrieval. Ignoring sub-pixel variations of cloud reflectances can lead to a significant bias in the retrieved τ and r_e. In the literature, the retrievals of τ and r_e are often assumed to be independent and considered separately when investigating the impact of sub-pixel cloud reflectance variations on the bi-spectral method. As a result, the impact on τ is contributed only by the sub-pixel variation of VIS/NIR band reflectance and the impact on r_e only by the sub-pixel variation of SWIR band reflectance.

In our new framework, we use the Taylor expansion of a two-variable function to understand and quantify the impacts of sub-pixel variances of VIS/NIR and SWIR cloud reflectances and their covariance on the τ and r_e retrievals. This framework takes into account the fact that the retrievals are determined by both VIS/NIR and SWIR band observations in a mutually dependent way. In comparison with previous studies, it provides a more comprehensive understanding of how sub-pixel cloud reflectance variations impact the τ and r_e retrievals based on the bi-spectral method. In particular, our framework provides a mathematical explanation of how the sub-pixel variation in VIS/NIR band influences the r_e retrieval and why it can sometimes outweigh the influence of variations in the SWIR band and dominate the error in r_e retrievals, leading to a potential contribution of positive bias to the r_e retrieval. We test our framework using synthetic cloud fields from a large-eddy simulation and real observations from MODIS. The predicted results based on our framework agree very well with the numerical simulations. Our framework can be used to estimate the retrieval uncertainty from sub-pixel reflectance variations in operational satellite cloud products and to help understand the differences in τ and r_e retrievals between two instruments.

1. Introduction

Among many satellite-based cloud remote sensing techniques, the bi-spectral solar reflective method ("bi-spectral method" hereafter) is a widely used method to infer cloud optical thickness (τ) and cloud droplet effective radius (r_e) from satellite observation of cloud reflectance [*Nakajima and King*, 1990]. This method uses cloud reflectance measurements from two spectral bands to simultaneously retrieve τ and r_e. One measurement is usually made in the visible or near-infrared (VIS/NIR) spectral region (e.g., 0.64 µm or 0.86 µm), where water absorption is negligible and therefore cloud reflection generally increases with τ. The other measurement is usually in the shortwave infrared (SWIR) spectral region (e.g., 2.1 µm or 3.7 µm), where water drops are moderately absorptive and cloud reflectance generally decreases with increasing r_e for optically thick clouds. In practice, the bi-spectral method is often implemented utilizing the so-called look-up-table (LUT). A couple of LUT examples are shown in Figure 1. Such LUTs contain pre-computed bi-directional cloud reflectances at VIS/NIR and SWIR bands for various combinations of r_e and τ under different sun-satellite viewing geometries and surface reflectances. Given the observed reflectances, the corresponding r_e and τ can be retrieved easily by searching and interpolating the proper LUT. The bi-spectral method has been adopted by a number of satellite missions, including Moderate Resolution Imaging Spectroradiometer (MODIS), Visible Infrared Imaging Radiometer Suite (VIIRS), and Spinning Enhanced Visible and Infrared Imager (SEVIRI) for operational retrievals of cloud properties (i.e., τ, r_e and derived cloud liquid water path (LWP)) [*Platnick et al.*, 2003; *Roebeling et al.*, 2006; *Minnis et al.*, 2011; *Walther and Heidinger*, 2012]. Given the wide usage of the bi-spectral method, it is critical to study and understand its limitations and uncertainties.

The bi-spectral method makes several important assumptions about the cloud (or cloudy pixels). First, within a cloudy pixel, cloud is assumed to be horizontally homogenous (referred to as the "homogenous pixel assumption"). Second, it is assumed that the pixels are independent from each other, in the sense that there is no net inter-pixel transport of radiation (often referred to as the "independent pixel assumption, IPA"). Under these assumptions, clouds are considered to be "plane-parallel". In addition to plane-parallel cloud assumptions, clouds are often assumed to be vertically homogenous in the operational algorithms. Furthermore, the size spectrum of cloud particles is often assumed to follow certain analytical distributions, such as the single modal gamma or lognormal size distributions [e.g., *Nakajima and King*, 1990; *Dong et al.*, 1997]. These assumptions may be reasonable for certain types of clouds, such as closed-cell, non-precipitating stratocumulus, but become problematic for others, such as broken trade-wind cumuli or precipitating clouds [*Di Girolamo et al.*, 2010; *Painemal and Zuidema*, 2011; *Zhang and Platnick*, 2011; *Liang and Girolamo*, 2013; *Zhang*, 2013]. As elucidated in numerous previous studies, when real clouds deviate from these assumptions, the r_e and τ retrievals from the bi-spectral method can suffer from large errors and uncertainties [e.g., *Várnai and Marshak*, 2002; *Kato et al.*, 2006; *Marshak et al.*, 2006; *Zhang and Platnick*, 2011; *Zhang et al.*, 2012; *Zhang*, 2013; *Liang et al.*, 2015].

The focus of this study is the homogenous pixel assumption. Our objective is to develop a unified framework for understanding and quantifying the impacts of sub-pixel level unresolved reflectance variations on r_e and τ retrievals based on the bi-spectral method. A number of previous studies have already made substantial progress in this direction. It has been known for a long time that at the spatial scale of climate model grids (e.g., ~ 10^2 km) approximating inhomogeneous cloud fields with plane-parallel clouds can lead to significant biases in shortwave solar radiation [e.g., *Harshvardhan and Randall*, 1985; *Cahalan et al.*, 1994; *Barker*, 1996]. *Cahalan et al.* [1994] described an elegant theoretical framework based on a fractal cloud model to explain the influence of small-scale horizontal variability of τ on the averaged cloud reflectance in the visible spectral region R_{VIS}. It is shown that the averaged reflectance $\overline{R_{VIS}(\tau_i)}$, where τ_i denotes the sub-pixel scale cloud optical thickness, is smaller than the reflectance that corresponds to the averaged cloud optical thickness $\overline{\tau_i}$, i.e., $\overline{R_{VIS}(\tau_i)} < R_{VIS}(\overline{\tau_i})$. This inequality relation is well known as the "plane-parallel homogenous bias" (referred to as PPHB), which is a result of the non-linear dependence of R_{VIS} on τ i.e., $\frac{\partial^2 R_{vis}}{\partial \tau^2} < 0$. The implication of the PPHB for τ retrievals from R_{VIS} is illustrated using an example shown in Figure 2a. Here, we assume that one half of an inhomogeneous pixel is covered by a thinner cloud with $\tau_1 = 5$ and the other half by a thicker cloud with $\tau_2 = 18$ (both clouds with $r_e = 8\mu m$). Because of the PPHB, the retrieved cloud optical thickness $\tau^* = 9.8$ based on the averaged reflectance

$\overline{R} = \left[R(\tau_1) + R(\tau_2) \right] / 2$ is significantly smaller than the linear average of the sub-pixel τ, i.e., $\overline{\tau} = 11.5$. The impacts of PPHB on satellite based cloud property retrievals and the implications have been investigated in a number of studies [*Oreopoulos and Davies*, 1998; *Pincus et al.*, 1999; *Oreopoulos et al.*, 2007].

We note that the variation of cloud reflectance may be a result of varying cloud properties, but may also be caused by 3-D radiative effects. For example, a cloudy pixel can be perfectly homogenous in terms of cloud properties, but the surrounding pixels can cast a shadow on part of this pixel leading to sub-pixel reflectance variation [*Marshak et al.*, 2006]. A variety of such 3-D effects that cannot be explained by the 1-D plane-parallel radiative transfer theory have been identified and their impacts on cloud property retrievals investigated in previous studies [*Davis and Marshak*, 2010]. In reality, the PPHB is inevitably entangled with the 3-D transfer effects and other uncertainties such as the impact of instrument noise in the retrieval. It is difficult, if not impossible, to separate them. Following the literature, we shall refer to the impact of sub-pixel cloud reflectance variation on cloud property retrievals as the PPHB, while keeping in mind that the sub-pixel cloud reflectance variation can also result from 3-D radiative effects and may not reflect the true variation of sub-pixel cloud properties.

Recently, as the interests in aerosol-cloud interactions have grown, there is an increasing attention on the impacts of small-scale cloud variations on the satellite-based r_e retrievals [e.g., *Kato et al.*, 2006; *Marshak et al.*, 2006; *Zhang and Platnick*, 2011; *Zhang et al.*, 2012; *Liang et al.*, 2015]. Marshak et al. [2006] pointed out that similar to the PPHB the non-linear dependence of the SWIR band cloud reflectance R_{SWIR} on r_e

can also lead to significant biases on r_e retrievals, which is demonstrated in Figure 2b. Here, one half of an inhomogeneous pixel is covered by a cloud with $r_e = 8\mu m$ and the other half by a cloud with $r_e = 22\mu m$. Both parts have the same $\tau = 4.1$. As shown in the figure, the retrieved $r_e^* = 12\mu m$ based on the averaged reflectance is significantly smaller than the linear average of sub-pixel $\overline{r_e} = 15\mu m$, similar to the PPHB of τ in Figure 2a. It must be noted that in the framework of Marshak et al. [2006] the retrievals of r_e and τ are considered separately and assumed to be independent from one another. However, as Marshak et al. [2006] pointed out this assumption is valid only for "large enough" τ and r_e (typically, r_e> 5 µm and τ > 10). As one can see from the shape of the LUT in Figure 1 the R_{SWIR} is not completely orthogonal to the R_{VIS}, especially when τ is small. As a result, the retrievals of r_e and τ are not independent from one another. Marshak et al. [2006] suspected that some cases with large r_e bias in their simulations might be the result of this mutual dependence of r_e and τ retrievals. Zhang and Platnick [2011] showed that the sub-pixel variance of τ can have a significant impact on the r_e retrieval, which is illustrated in the example in Figure 2c. In this hypothetical case, an inhomogeneous pixel is assumed to be covered by a thinner cloud with τ_1=6 in one half and a thicker cloud with τ_2=18 in the other. Both clouds have the same r_e=14 µm. Note that in this case the sub-pixel reflectance variation is solely caused by the variability in τ. If the r_e retrieval were independent from the τ retrieval, then the retrieved r_e would be 14 µm. The solid triangle in the figure indicates the location of the R_{VIS} and R_{SWIR} averaged over the pixel, i.e., the "observation". The retrieved $\tau^* = 10.8$

is smaller than the averaged $\bar{\tau} = 12$ as a result of the PPHB. However, the retrieved $r_e^* = 16$ is 2 µm larger than the expected value of 14 µm. This positive bias in the r_e retrieval, apparently caused by the sub-pixel variability of τ, cannot be explained by the framework of Marshak et al. [2006] in which the r_e retrieval is assumed to be independent from the τ retrieval. Zhang and Platnick [2011] and Zhang et al. [2012] also found that the magnitude of the positive r_e retrieval bias caused by the sub-pixel variability of τ is dependent on the SWIR band chosen for the r_e retrieval. These studies showed that the same sub-pixel τ variability tends to induce larger bias in retrieved r_e using the less absorptive 2.1 µm band (referred to as $r_{e,2.1}$) than that using the more absorptive 3.7 µm band (referred to as $r_{e,3.7}$). This spectral dependence provides an important explanation for the fact that the MODIS operational $r_{e,2.1}$ retrievals for water clouds are often significantly larger than the $r_{e,3.7}$ retrievals, especially when clouds have large sub-pixel heterogeneity [*Zhang and Platnick*, 2011; *Cho et al.*, 2015].

The aforementioned studies have undoubtedly shed important light on the impact of sub-pixel cloud variability on r_e and τ retrievals based on the bi-spectral method. However, several questions still remain. For example, an important question is how to reconcile the negative r_e bias discussed in Marshak et al. [*Marshak et al.*, 2006] and the positive r_e bias discussed in Zhang and Platnick [2011] and Zhang et al. [2012]. Indeed, this is the main question we will address in this study. In the light of previous studies, here we develop a new mathematical framework to provide a more comprehensive and complete understanding of the impact of sub-pixel cloud variability on r_e and τ retrievals based on the bi-spectral method. The paper is organized as follows: We formulate the problem in Section 2. We introduce our mathematical framework in Section 3, test and validate it using two examples in Section 4, and discuss its applications in Section 5.

2. Statement of the problem

In the bi-spectral method, r_e and τ are retrieved from a pair of cloud reflectance observations, one in VIS/NIR and the other in SWIR. From this point of view, we can define r_e and τ as:

$$\begin{aligned} \tau &\equiv \tau\left(R_{VIS}, R_{SWIR}\right) \\ r_e &\equiv r_e\left(R_{VIS}, R_{SWIR}\right) \end{aligned}, \quad (1)$$

where R_{VIS} and R_{SWIR} are the observed reflectances in the VIS/NIR (denoted by subscript "VIS" for short) and SWIR bands, respectively. Assume that an instrument with a relatively coarse spatial resolution observes a horizontally inhomogeneous cloudy pixel in its field of view. The observed cloud reflectances are $\overline{R_{VIS}}$ and $\overline{R_{SWIR}}$, where the overbar denotes the spatial average. Now if we use another instrument with a finer spatial resolution to observe the same area covered by the coarser resolution pixel, we can obtain high-resolution observations, $R_{VIS,i}$ and $R_{SWIR,i}, i = 1, 2, \ldots N$, (the number *N* depends on the relative sizes of the pixels). The high-resolution measurements provide the information on the variance and covariance of R_{VIS} and R_{SWIR} at sub-pixel scale. Each sub-pixel observation $R_{VIS,i}$ and $R_{SWIR,i}$ can be specified as the deviation from the mean value $\overline{R_{VIS}}$ and $\overline{R_{SWIR}}$ as:

$$\begin{aligned} R_{VIS,i} &= \overline{R_{VIS}} + \Delta R_{VIS,i} \\ R_{SWIR,i} &= \overline{R_{SWIR}} + \Delta R_{SWIR,i} \end{aligned} \quad ; i = 1,2...N . \tag{2}$$

It naturally follows that the spatial average $\overline{\Delta R_{VIS,i}} = \overline{\Delta R_{SWIR,i}} = 0$. Based on the coarse-resolution reflectance observations $\overline{R_{VIS}}$ and $\overline{R_{SWIR}}$, we can retrieve $\tau\left(\overline{R_{VIS}}, \overline{R_{SWIR}}\right)$ and $r_e\left(\overline{R_{VIS}}, \overline{R_{SWIR}}\right)$. From the high-resolution, sub-pixel observations $R_{VIS,i}$ and $R_{SWIR,i}$, we can retrieve $\tau\left(R_{VIS,i}, R_{SWIR,i}\right)$ and $r_e\left(R_{VIS,i}, R_{SWIR,i}\right)$. The differences $\Delta\tau$ and Δr_e, defined as:

$$\begin{aligned} \Delta\tau &= \tau\left(\overline{R_{VIS}}, \overline{R_{SWIR}}\right) - \overline{\tau\left(R_{VIS,i}, R_{SWIR,i}\right)} \\ \Delta r_e &= r_e\left(\overline{R_{VIS}}, \overline{R_{SWIR}}\right) - \overline{r_e\left(R_{VIS,i}, R_{SWIR,i}\right)} \end{aligned}, \tag{3}$$

are considered in this, as well as previous studies, as the biases caused by the homogeneous pixel assumption in r_e and τ retrievals [*Cahalan and Joseph*, 1989; *Marshak et al.*, 2006; *Zhang et al.*, 2012].

Consideration of eq. (3) raises a few important questions. What are the sign and magnitude of $\Delta\tau$ and Δr_e? How do they depend on the sub-pixel $R_{VIS,i}$ and $R_{SWIR,i}$? Addressing these questions could help improve understanding of the biases caused by ignoring the sub-pixel reflectance variation in bi-spectral r_e and τ retrievals. Furthermore, since performing high-resolution retrievals can be computationally expensive, another important question is whether it is possible to estimate $\overline{\tau\left(R_{VIS,i}, R_{SWIR,i}\right)}$ and $\overline{r_e\left(R_{VIS,i}, R_{SWIR,i}\right)}$ from the coarse-resolution retrievals and the statistics of sub-pixel reflectance observations, even without doing time-consuming high-resolution retrievals. If this proved possible, then it is a very efficient way to estimate the biases and uncertainty caused by the homogenous pixel assumption. These questions are the focus of this study and will be addressed in the next section.

Before proceeding, we need to clarify two points. First, the $\Delta\tau$ and Δr_e in Eq. (3) are the differences between two sets of retrievals, *not* the differences between the retrievals and “true” cloud properties. As aforementioned, sub-pixel reflectance variations can be due to sub-pixel scale cloud property variation, but may also be caused by 3-D radiative effects. If the former is dominant, then $\Delta\tau$ and Δr_e provide an estimate of the PPHB and can be used to correct the coarse-resolution retrievals to better represent the “true” cloud properties. However, if 3-D effects are the dominant cause of the sub-pixel reflectance variation, then $\Delta\tau$ and Δr_e can be considered a quantitative index of the 3-D effects on the retrievals. Second, our scope is to study the connections between retrieval biases $\Delta\tau$ and Δr_e with sub-pixel observations $R_{VIS,i}$ and $R_{SWIR,i}$. We simply take $R_{VIS,i}$ and $R_{SWIR,i}$ as given inputs. Here we do *not* seek to explain the characteristics of $R_{VIS,i}$ and $R_{SWIR,i}$ (e.g., their mean values, variances and covariance), or their dependence on cloud properties. Neither do we try to explain how the 3-D radiative effects and instrument characteristics influence $R_{VIS,i}$ and $R_{SWIR,i}$.

3. A unified mathematical framework

In this section, we will introduce a comprehensive framework that is able to reconcile and unify the theoretical understandings provided by Marshak et al. [2006] , Zhang and Platnick [2011], and Zhang et al. [2012] To investigate the sign and magnitude of $\Delta\tau$ and Δr_e, we first expand the $\tau\left(R_{VIS,i}, R_{SWIR,i}\right)$ and $r_e\left(R_{VIS,i}, R_{SWIR,i}\right)$ into two-dimensional Taylor series of $R_{VIS,i}$ and $R_{SWIR,i}$. Take $r_e\left(R_{VIS,i}, R_{SWIR,i}\right)$ for example. The expansion is:

$$\begin{aligned} r_e\left(R_{VIS,i}, R_{SWIR,i}\right) &= r_e\left(\overline{R_{VIS}} + \Delta R_{VIS,i}, \overline{R_{SWIR}} + \Delta R_{SWIR,i}\right) \\ &= r_e\left(\overline{R_{VIS}}, \overline{R_{SWIR}}\right) + \underbrace{\frac{\partial r_e\left(\overline{R_{VIS}}, \overline{R_{SWIR}}\right)}{\partial R_{VIS}}\Delta R_{VIS,i} + \frac{\partial r_e\left(\overline{R_{VIS}}, \overline{R_{SWIR}}\right)}{\partial R_{SWIR}}\Delta R_{SWIR,i}}_{\text{Linear terms}} + \\ &\underbrace{\frac{1}{2}\frac{\partial^2 r_e\left(\overline{R_{VIS}}, \overline{R_{SWIR}}\right)}{\partial R_{VIS}^2}\Delta R_{VIS,i}^2 + \frac{\partial^2 r_e\left(\overline{R_{VIS}}, \overline{R_{SWIR}}\right)}{\partial R_{VIS}\,\partial R_{SWIR}}\Delta R_{VIS,i}\Delta R_{SWIR,i} + \frac{1}{2}\frac{\partial^2 r_e\left(\overline{R_{VIS}}, \overline{R_{SWIR}}\right)}{\partial R_{SWIR}^2}\Delta R_{SWIR,i}^2}_{\text{Second-order terms}} + \varepsilon \end{aligned} \quad . (4)$$

where ε is the truncation error if higher order derivative terms are neglected. If we take the spatial average of Eq. (4) and neglect ε, all the linear terms (i.e., $\frac{\partial r_e\left(\overline{R_{VIS}}, \overline{R_{SWIR}}\right)}{\partial R_{VIS}}\Delta R_{VIS,i}$ and $\frac{\partial r_e\left(\overline{R_{VIS}}, \overline{R_{SWIR}}\right)}{\partial R_{SWIR}}\Delta R_{SWIR,i}$) vanish because $\overline{\Delta R_{VIS,i}} = \overline{\Delta R_{SWIR,i}} = 0$. Thus, only second order terms in Eq. (4) remain after the spatial average:

$$\overline{r_e\left(R_{VIS,i}, R_{SWIR,i}\right)} \approx r_e\left(\overline{R_{VIS}}, \overline{R_{SWIR}}\right) + \frac{1}{2}\frac{\partial^2 r_e\left(\overline{R_{VIS}}, \overline{R_{SWIR}}\right)}{\partial R_{VIS}^2}\sigma_{VIS}^2 + \frac{\partial^2 r_e\left(\overline{R_{VIS}}, \overline{R_{SWIR}}\right)}{\partial R_{VIS}\,\partial R_{SWIR}}\operatorname{cov}\left(R_{VIS}, R_{SWIR}\right) + \frac{1}{2}\frac{\partial^2 r_e\left(\overline{R_{VIS}}, \overline{R_{SWIR}}\right)}{\partial R_{SWIR}^2}\sigma_{SWIR}^2 ,$$

(5)

where $\sigma_{VIS}^2 = \overline{\Delta R_{VIS,i}^2}$, $\sigma_{SWIR}^2 = \overline{\Delta R_{SWIR,i}^2}$ are the spatial variances of $R_{VIS,i}$ and $R_{SWIR,i}$, respectively, and $\operatorname{cov}\left(R_{VIS}, R_{SWIR}\right)$ is the spatial covariance of $R_{VIS,i}$ and $R_{SWIR,i}$. Substituting Eq. (5) into Eq. (3), we obtain the following formula for Δr_e:

$$\begin{aligned}\Delta r_e &= r_e\left(\overline{R_{VIS}},\overline{R_{SWIR}}\right)-\overline{r_e\left(R_{VIS,i},R_{SWIR,i}\right)}\\ &= -\frac{1}{2}\frac{\partial^2 r_e\left(\overline{R_{VIS}},\overline{R_{SWIR}}\right)}{\partial R_{VIS}^2}\sigma_{VIS}^2-\frac{\partial^2 r_e\left(\overline{R_{VIS}},\overline{R_{SWIR}}\right)}{\partial R_{VIS}\,\partial R_{SWIR}}\mathrm{cov}\left(R_{VIS},R_{SWIR}\right)-\frac{1}{2}\frac{\partial^2 r_e\left(\overline{R_{VIS}},\overline{R_{SWIR}}\right)}{\partial R_{SWIR}^2}\sigma_{SWIR}^2\end{aligned} \tag{6}$$

Following the same procedure, we can derive the formula for $\Delta\tau$ as:

$$\begin{aligned}\Delta\tau &= \tau\left(\overline{R_{VIS}},\overline{R_{SWIR}}\right)-\overline{\tau\left(R_{VIS,i},R_{SWIR,i}\right)}\\ &= -\frac{1}{2}\frac{\partial^2 \tau\left(\overline{R_{VIS}},\overline{R_{SWIR}}\right)}{\partial R_{VIS}^2}\sigma_{VIS}^2-\frac{\partial^2 \tau\left(\overline{R_{VIS}},\overline{R_{SWIR}}\right)}{\partial R_{VIS}\,\partial R_{SWIR}}\mathrm{cov}\left(R_{VIS},R_{SWIR}\right)-\frac{1}{2}\frac{\partial^2 \tau\left(\overline{R_{VIS}},\overline{R_{SWIR}}\right)}{\partial R_{SWIR}^2}\sigma_{SWIR}^2\end{aligned} \tag{7}$$

Eq. (6) and (7) can be combined into a matrix form as follows:

$$\begin{pmatrix}\Delta\tau\\ \Delta r_e\end{pmatrix}=\begin{pmatrix}-\frac{1}{2}\frac{\partial^2 \tau\left(\overline{R_{VIS}},\overline{R_{SWIR}}\right)}{\partial R_{VIS}^2} & -\frac{\partial^2 \tau\left(\overline{R_{VIS}},\overline{R_{SWIR}}\right)}{\partial R_{VIS}\,\partial R_{SWIR}} & -\frac{1}{2}\frac{\partial^2 \tau\left(\overline{R_{VIS}},\overline{R_{SWIR}}\right)}{\partial R_{SWIR}^2}\\ -\frac{1}{2}\frac{\partial^2 r_e\left(\overline{R_{VIS}},\overline{R_{SWIR}}\right)}{\partial R_{VIS}^2} & -\frac{\partial^2 r_e\left(\overline{R_{VIS}},\overline{R_{SWIR}}\right)}{\partial R_{VIS}\,\partial R_{SWIR}} & -\frac{1}{2}\frac{\partial^2 r_e\left(\overline{R_{VIS}},\overline{R_{SWIR}}\right)}{\partial R_{SWIR}^2}\end{pmatrix}\begin{pmatrix}\sigma_{VIS}^2\\ \mathrm{cov}\\ \sigma_{SWIR}^2\end{pmatrix}. \tag{8}$$

Eq. (8) is the central equation of our framework for quantifying the impact of sub-pixel reflectance variance on r_e and τ retrievals. Eq. (8) decomposes the impact of sub-pixel cloud reflectance variability on the τ and r_e retrievals based on the bi-spectral method into two parts: 1) the magnitude of the sub-pixel reflectance variance and covariance specified by the vector $\left(\sigma_{VIS}^2,\ \mathrm{cov},\ \sigma_{SWIR}^2\right)^T$ (referred to as "sub-pixel variance vector") and 2) the matrix of the second-order derivatives of the LUT with respect to R_{VIS} and R_{SWIR} (referred to as "matrix of 2nd derivatives"). Given the LUT, the matrix of 2nd derivatives can be easily derived from straightforward numerical differentiation. An example of such a derived matrix based on the LUT for 0.86 µm reflectance ($R_{0.86}$) and 2.1 µm reflectance ($R_{2.1}$) is shown in Figure 3. The values of the 2nd derivatives for the grids of LUT are indicated by the color bar. Note that the sign of $\Delta\tau$ or Δr_e is determined both by the 2nd derivatives and the sub-pixel variance vector $\left(\sigma_{VIS}^2,\ \mathrm{cov},\ \sigma_{SWIR}^2\right)^T$. While σ_{VIS}^2 and σ_{SWIR}^2 are positive definite, the covariance term can be negative.

It is clear from Eq. (8) that the τ and r_e retrievals are not only influenced by the sub-pixel variation of the primary band (i.e., R_{VIS} for τ and R_{SWIR} for r_e) but also by the variation of the secondary band (i.e., R_{SWIR} for τ and R_{VIS} for r_e), as well as the covariance of the two bands R_{VIS} and R_{SWIR}. Therefore, it reconciles and unifies the theoretical frameworks in Marshak et al. [2006] and Zhang and Platnick [*Zhang and Platnick*, 2011] and Zhang et al. [2012]. In particular, the impact of the PPHB on τ and r_e , described in Marshak et al. [2006], corresponds to the upper-left term, $-\frac{1}{2}\frac{\partial^2\tau\left(\overline{R_{VIS}},\overline{R_{SWIR}}\right)}{\partial R_{VIS}^2}$ (Figure 3a), and lower-right term, $-\frac{1}{2}\frac{\partial^2 r_e\left(\overline{R_{VIS}},\overline{R_{SWIR}}\right)}{\partial R_{SWIR}^2}$ (Figure 3f), in the 2nd derivatives matrix, respectively. As shown in Figure 3, both terms are generally negative over the most part of LUT, consistent with the finding of Marshak et al. [2006] that ignoring sub-pixel variability tends to result in an underestimation of the pixel average of the retrieved quantity if τ and r_e retrievals are considered separately and independently (i.e., negative $\Delta\tau$ and Δr_e). On the other hand, $\Delta\tau$ and Δr_e are also influenced by other terms in the matrix. Physically, these terms arise from the fact that both R_{VIS} and R_{SWIR} depend not only on τ but also r_e . For example, the $-\frac{1}{2}\frac{\partial^2 r_e\left(\overline{R_{VIS}},\overline{R_{SWIR}}\right)}{\partial R_{VIS}^2}$ term in Figure 3d is mostly positive in the region of the LUT with τ between about 1.5 and 20 and r_e between about 10 and 28 µm. This term competes with the negative $-\frac{1}{2}\frac{\partial^2 r_e\left(\overline{R_{VIS}},\overline{R_{SWIR}}\right)}{\partial R_{SWIR}^2}$ term in determining the sign and size of Δr_e. In some cases, when σ_{VIS}^2 is large as in the example in Figure 2c, the influence of $-\frac{1}{2}\frac{\partial^2 r_e\left(\overline{R_{VIS}},\overline{R_{SWIR}}\right)}{\partial R_{VIS}^2}$ may be stronger, leading to a positive Δr_e, as argued in Zhang and Platnick [2011] and Zhang et al. [2012].

Some new terms that have not been explained in previous studies, e.g., the cross terms $-\frac{\partial^2 \tau\left(\overline{R_{VIS}},\overline{R_{SWIR}}\right)}{\partial R_{VIS}\,\partial R_{SWIR}}$ in Figure 3b and $-\frac{\partial^2 r_e\left(\overline{R_{VIS}},\overline{R_{SWIR}}\right)}{\partial R_{VIS}\,\partial R_{SWIR}}$ in Figure 3e, also emerge from Eq. (8). These two terms generally have the opposite sign of $-\frac{1}{2}\frac{\partial^2 \tau\left(\overline{R_{VIS}},\overline{R_{SWIR}}\right)}{\partial R_{VIS}^2}$ and $-\frac{1}{2}\frac{\partial^2 r_e\left(\overline{R_{VIS}},\overline{R_{SWIR}}\right)}{\partial R_{SWIR}^2}$. Because the covariance cov is generally positive, the cross terms evidently counteract the effects of $-\frac{1}{2}\frac{\partial^2 \tau\left(\overline{R_{VIS}},\overline{R_{SWIR}}\right)}{\partial R_{VIS}^2}$ and $-\frac{1}{2}\frac{\partial^2 r_e\left(\overline{R_{VIS}},\overline{R_{SWIR}}\right)}{\partial R_{SWIR}^2}$ on $\Delta\tau$ and Δr_e.

Eq. (8) also provides a quantitative explanation for why sub-pixel inhomogeneity has different impacts on the r_e retrievals based on different SWIR bands (i.e., $r_{e,2.1}$ vs. $r_{e,3.7}$). Figure 4 shows an example of the matrix of 2nd derivatives for the $R_{0.86}$ and $R_{3.7}$

combination. In comparison with the $R_{0.86}$ and $R_{2.1}$ combination in Figure 3, the $-\frac{1}{2}\frac{\partial^2 r_e\left(\overline{R_{VIS}},\overline{R_{SWIR}}\right)}{\partial R_{VIS}^2}$ term in Figure 4d is significantly smaller. This suggests that the same sub-pixel inhomogeneity in the 0.86 µm band (i.e., same σ_{VIS}^2) has a stronger impact on $r_{e,2.1}$ than it does on $r_{e,3.7}$. Because this term tends to lead to a positive Δr_e bias, it could be an important reason why the MODIS $r_{e,2.1}$ retrievals are often found to be significantly larger than the $r_{e,3.7}$, in particular for inhomogeneous pixels [*Painemal and Zuidema*, 2011; *Zhang and Platnick*, 2011; *Zhang et al.*, 2012; *Cho et al.*, 2015].

As analyzed above, in comparison with previous studies the framework described in Eq. (8) provides us with a more comprehensive explanation of the bias in τ and r_e retrievals caused by the homogenous pixel assumption. This framework may be useful in a variety of applications. It can be used to quantify $\Delta\tau$ and Δr_e if the sub-pixel variances and covariance $\left(\sigma_{VIS}^2,\ \mathrm{cov},\ \sigma_{SWIR}^2\right)^T$ are known, as shown in the example in the next section. The $\Delta\tau$ and Δr_e can then in turn be used to estimate the uncertainties and potential biases in τ and r_e retrievals due to ignoring the sub-pixel reflectance variability in the bi-spectral method. Our framework can also be used to understand the differences among retrievals based on instruments with different spatial resolutions.

Finally, it is worth mentioning that Eq. (8) can be rewritten in a slightly different form as follows:

$$\begin{pmatrix} \Delta\tau \\ \Delta r_e \end{pmatrix} = \begin{pmatrix} -\frac{1}{2}\frac{\partial^2 \tau\left(\overline{R_{VIS}},\overline{R_{SWIR}}\right)}{\partial R_{VIS}^2}\left(\overline{R_{VIS}}\right)^2 & -\frac{\partial^2 \tau\left(\overline{R_{VIS}},\overline{R_{SWIR}}\right)}{\partial R_{VIS}\,\partial R_{SWIR}}\left(\overline{R_{VIS}}\cdot\overline{R_{SWIR}}\right) & -\frac{1}{2}\frac{\partial^2 \tau\left(\overline{R_{VIS}},\overline{R_{SWIR}}\right)}{\partial R_{SWIR}^2}\left(\overline{R_{SWIR}}\right)^2 \\ -\frac{1}{2}\frac{\partial^2 r_e\left(\overline{R_{VIS}},\overline{R_{SWIR}}\right)}{\partial R_{VIS}^2}\left(\overline{R_{VIS}}\right)^2 & -\frac{\partial^2 r_e\left(\overline{R_{VIS}},\overline{R_{SWIR}}\right)}{\partial R_{VIS}\,\partial R_{SWIR}}\left(\overline{R_{VIS}}\cdot\overline{R_{SWIR}}\right) & -\frac{1}{2}\frac{\partial^2 r_e\left(\overline{R_{VIS}},\overline{R_{SWIR}}\right)}{\partial R_{SWIR}^2}\left(\overline{R_{SWIR}}\right)^2 \end{pmatrix} \begin{pmatrix} H_{\sigma_{VIS}}^2 \\ H_{\mathrm{cov}} \\ H_{\sigma_{SWIR}}^2 \end{pmatrix} \tag{9}$$

where $H_{\sigma_{VIS}}^2 = \sigma_{VIS}^2 / \left(\overline{R_{VIS}}\right)^2$, $H_{\sigma_{SWIR}}^2 = \sigma_{SWIR}^2 / \left(\overline{R_{SWIR}}\right)^2$, and $H_{COV} = \mathrm{cov}\left(R_{VIS}, R_{SWIR}\right) / \left(\overline{R_{VIS}} \cdot \overline{R_{SWIR}}\right)$. Note that $H_{\sigma_{VIS}}$ has been used in previous studies as an index of sub-pixel inhomogeneity, in particular for MODIS cloud retrievals [e.g., *Liang et al.*, 2009; *Di Girolamo et al.*, 2010; *Zhang and Platnick*, 2011; *Zhang et al.*, 2012; *Cho et al.*, 2015]. Therefore, although Eq. (9) and (8) are equivalent, some readers may find $\left(H_{\sigma_{VIS}}^2, H_{\mathrm{cov}}, H_{\sigma_{SWIR}}^2\right)^T$ more familiar than $\left(\sigma_{VIS}^2,\ \mathrm{cov},\ \sigma_{SWIR}^2\right)^T$.

It is important to point out that Eqs. (8)-(9) hold, no matter whether the sub-pixel reflectance variations (i.e., non-zero $\left(\sigma_{VIS}^2,\ \mathrm{cov},\ \sigma_{SWIR}^2\right)^T$) are attributable to sub-pixel scale cloud property variations, 3-D radiative effects, or both. It is the interpretation of the resultant $\Delta\tau$ and Δr_e that is dependent on the circumstances and needs to be made with caution.

Finally, it is important to note that a critical assumption in our derivation is that the truncation error ε in the Taylor expansion is negligible. This term is a summation of all the higher order derivatives. Take r_e for example, the form of the k^{th} order derivative:

$$\frac{1}{k!}\frac{d^k r_e}{dR^k} = \sum_{0\le m\le k} \frac{1}{m!(k-m)!}\frac{\partial^k r_e}{\partial R_{vis}^m \partial R_{vis}^{k-m}}\left(\overline{R_{VIS}}, \overline{R_{SWIR}}\right)\Delta R_{VIS}^m \Delta R_{SWIR}^{k-m}. \quad (10)$$

Because there is no analytical solution to the higher order derivatives, we can only assess the validity of this assumption and evaluate the accuracy of our framework numerically, which is done in the next section.

4. Numerical tests

In this section, we evaluate the accuracy and limits of our mathematical framework using two examples. The main objective is to assess, through case studies, if the higher order derivative terms are negligible so that our framework in Eq. (8) provides an accurate estimate of the PPHB.

4.1. Cloud fields from large-eddy simulation

In the first example, we test our framework using a synthetic cloud field simulated from a large-eddy simulations (LES) model (DHARMA) with bin microphysics [*Ackerman et al.*, 2004]. The LES case is based on an idealized case study [*Stevens et al.*, 2010] from the Atlantic Trade Wind Experiment (ATEX), with an diagnostic treatment of aerosol, specified to have a uniform number concentration of 40 cm^{-3}. The ATEX simulation represents a trade-wind cumulus case under a sharp inversion. The ATEX simulation has a domain size of 9.6 x 9.6 x 3 km, with a uniform horizontal grid of Δx=Δy=100 m and a fixed vertical grid spacing of Δz=40 m. Further details of the model setup for the LES case are provided in Zhang et al. [2012]. The droplet size distributions from the LES are used to drive the radiative transfer simulations. The solar zenith and azimuth angle are set at 20° and 30°, respectively, for the radiative transfer simulations. For simplicity, the surface is assumed to be black. Both 1-D and 3-D radiative transfer simulations were performed, using the DISORT [*Stamnes et al.*, 1988] and the I3RC model [*Pincus and Evans*, 2009], respectively. We focus on the 3-D results because they are more representative of real retrievals. The 1-D results are similar and are therefore not shown here.

We first run radiative transfer simulations at the 100-m horizontal resolution of the LES grid. Figure 5a—c show the simulated 100-m cloud bi-directional reflectances at nadir viewing angle for the 0.86, 2.1, and 3.7 µm MODIS bands, receptively. Then, the 100m reflectances are aggregated to 400 m to simulate the coarse-resolution observations, which are shown in Figure 5d—f. Obviously, for each 400-m pixel we have 4x4 100m pixels that can be used to derive the variances and covariances of sub-pixel reflectance variances. Figure 6 shows the sub-pixel reflectance variances, $\sigma_{0.86}^2$, $\sigma_{2.1}^2$ and $\sigma_{3.7}^2$, and covariances, $\operatorname{cov}(R_{0.86}, R_{2.1})$ and $\operatorname{cov}(R_{0.86}, R_{3.7})$ derived from 100-m reflectances. Because of the large, order-of-magnitude differences between $R_{0.86}$, $R_{2.1}$ and $R_{3.7}$, $\sigma_{0.86}^2$ is substantially larger than $\sigma_{2.1}^2$, which in turn is substantially larger than $\sigma_{3.7}^2$. Both covariances $\operatorname{cov}(R_{0.86}, R_{2.1})$ and $\operatorname{cov}(R_{0.86}, R_{3.7})$ are generally positive, indicating a general positive correlation between SWIR and VIS/NIR band cloud reflectances. This is not surprising because $R_{2.1}$ and $R_{3.7}$ do increase with τ when the cloud is optically thin. Only for optically thick clouds do $R_{2.1}$ and $R_{3.7}$ become independent from $R_{0.86}$. Figure 7 shows the reflectance variances and covariances normalized by the mean reflectances squared, i.e., $H_{\sigma_{0.86}}^2$, $H_{\sigma_{2.1}}^2$ and $H_{\sigma_{3.7}}^2$ and

$\mathrm{cov}\left(R_{0.86},R_{2.1}\right)/\left(\overline{R_{0.86}},\cdot\overline{R_{2.1}}\right)$ and $\mathrm{cov}\left(R_{0.86},R_{3.7}\right)/\left(\overline{R_{0.86}}\cdot\overline{R_{3.7}}\right)$. After the normalization, $H^2_{\sigma_{0.86}}$, $H^2_{\sigma_{2.1}}$ and $H^2_{\sigma_{3.7}}$ are more comparable in terms of magnitude. In addition, cloud edges are seen to have larger sub-pixel inhomogeneity than the center of the cloud, which has also been found in MODIS observations [*Zhang and Platnick*, 2011; *Liang and Girolamo*, 2013].

The τ retrievals based on the simulated 100-m cloud reflectances ($R_{0.86}$ and $R_{2.1}$ combination) in Figure 5a—b are shown in Figure 8a, which closely follow the $R_{0.86}$ observations in Figure 5a. The τ retrievals based on the $R_{0.86}$ and $R_{3.7}$ combination are mostly identical and therefore not shown. The $r_{e,2.1}$ and $r_{e,3.7}$ retrievals based on the 100-m reflectances are shown in Figure 8b—c. For consistency with the notation in Section 3, we refer to these retrievals as sub-pixel retrievals, i.e., $\tau\left(R_{0.86,i},R_{2.1,i}\right)$, $r_e\left(R_{0.86,i},R_{2.1,i}\right)$ and $r_e\left(R_{0.86,i},R_{3.7,i}\right)$. The τ, $r_{e,2.1}$ and $r_{e,3.7}$ retrievals based on the aggregated 400m reflectances in Figure 5d—f are shown in Figure 8d—f, respectively, which are referred to as pixel-level retrievals $\tau\left(\overline{R_{0.86,i}},\overline{R_{2.1,i}}\right)$, $r_e\left(\overline{R_{0.86,i}},\overline{R_{2.1,i}}\right)$ and $r_e\left(\overline{R_{0.86,i}},\overline{R_{3.7,i}}\right)$.

Having derived both sub-pixel and pixel level retrievals, we first compute the biases caused by the homogenous pixel assumption, $\Delta\tau$ and Δr_e, as expressed in Eq. (3). The results are shown in Figure 9a—c. It can be seen that $\Delta\tau$ is mostly negative over the whole domain, as one would expect based on the PPHB. However, the Δr_e, especially $\Delta r_{e,2.1}$, is predominantly positive, which is the opposite of PPHB but consistent with the findings in Zhang and Platnick [2011] and Zhang et al. [2012]. It should be pointed out that the cloud-free pixels are marked in black in the figure. The pixels in gray are partly cloudy pixels (i.e., one or more 100-m sub-pixels are cloud-free). (Because it is uncertain how cloud-free sub-pixels should be treated in the spatial averages, partly cloudy pixels are excluded from our analysis.)

To assess the accuracy of our framework, we derived the second set of $\Delta\tau$ and Δr_e based on Eq. (8) using the matrix of 2nd derivatives (Figure 3 andFigure 4) and the sub-pixel reflectance variances and covariances (Figure 6). The results from this method are shown in Figure 9d—f. Evidently, $\Delta\tau$ and Δr_e derived in two different and independent ways agree very well. The correlation coefficients all exceed 0.8 as shown in Figure 9g—i. Only those pixels with large sub-pixel inhomogeneity index $H_{\sigma_{0.86}}$ (>0.5) deviate from the one-to-one line. For these pixels the higher order terms $O\left(\Delta R^3\right)$ ignored in Eq. (8), likely impact $\Delta\tau$ and Δr_e. But such cases are relatively rare for this LES scene. The overall excellent agreement clearly demonstrates that our framework is able to provide an accurate quantitative estimation of the biases in τ and r_e retrievals caused by the homogenous pixel assumption for overcast pixels.

An advantage of using Eq. (8) is that the bias can be further decomposed into the contributions from each term in the matrix of 2nd derivatives, which help us to better understand the relative importance of various factors in causing the bias. For example, as shown in Figure 10a—c, the τ retrieval bias is dominated by the $-\frac{1}{2}\frac{\partial^2\tau\left(\overline{R_{VIS}},\overline{R_{SWIR}}\right)}{\partial R_{VIS}^2}\cdot\sigma_{VIS}^2$ term in Eq. (7). As mentioned before, this term corresponds to the PPHB (Figure 2a), which is why the total $\Delta\tau$ in Figure 9 is generally negative. In the case of the $r_{e,3.7}$ retrieval, both the positive $-\frac{1}{2}\frac{\partial^2 r_e\left(\overline{R_{VIS}},\overline{R_{SWIR}}\right)}{\partial R_{VIS}^2}\cdot\sigma_{VIS}^2$ term (Figure 10g) and the negative $-\frac{1}{2}\frac{\partial^2 r_e\left(\overline{R_{VIS}},\overline{R_{SWIR}}\right)}{\partial R_{SWIR}^2}\cdot\sigma_{SWIR}^2$ term (Figure 10i) are significant. The former corresponds to the example in Figure 2c, while the latter refers to the example in Figure 2b. After summation, the $-\frac{1}{2}\frac{\partial^2 r_e\left(\overline{R_{VIS}},\overline{R_{SWIR}}\right)}{\partial R_{VIS}^2}\sigma_{VIS}^2$ is dominant and leads to the overall positive bias in the $r_{e,3.7}$ retrieval. The bias in the $r_{e,2.1}$ retrieval is even more complicated, as all three terms on the right hand side of Eq. (6) contribute substantially to the bias. Overall, the positive terms in Figure 10d—e dominate the total error budget, leading to a generally positive $\Delta r_{e,2.1}$ in Figure 8.

In the above example, the solar zenith angle is high, with $\theta_0 = 20$ °. We also tested our framework in a case with low solar zenith angle of $\theta_0 = 60$ ° and the results are shown in Figure 11. The correlations between the biases from the numerical simulations and those predicted by our framework are substantial, suggesting our framework works equally well for a high sun in this case.

From the above example, one can clearly see that our framework provides a comprehensive explanation of the impact of sub-pixel inhomogeneity on τ and r_e retrievals. As mentioned earlier we have also tested our framework on the retrievals based on reflectance using 1-D radiative transfer, and find the predicted $\Delta\tau$ and Δr_e based on our framework to agree very well with the numerical results (not shown).

We'd like to point out here that less sensitivity to sub-pixel heterogeneity in the 3.7µm channel should not necessarily be equated to less r_e bias in the overall retrieval. For simplicity, our 3.7 µm analysis deals with reflectance only. Thus it assumes that the cloud and surface temperatures are known without error, as are the atmospheric emission/correction terms, needed to infer cloud top reflectance from top-of-atmosphere measurements of emitted and reflected radiation. Because we are dealing with reflectance only, it is implicitly assumed that the effects of sub-pixel heterogeneity on the cloud temperature retrieval and atmospheric correction are negligible. The validity of this assumption will be assessed in future work.

4.2. MODIS retrieval test

In the second example, we test our framework using MODIS observations. The MODIS instrument has 36 spectral bands. The spatial resolution of most bands (bands 8—36) is 1 km. Bands 3—7 have a 500-m resolution. Bands 1 and 2 have a 250 m spatial resolution. The current (collection 06) operational MODIS cloud property retrieval products, such as τ, r_e and LWP, are made at 1-km resolution. The higher spatial resolution of the 0.86 µm (band 2) and 2.1 µm (band 7) sensors provides us with an opportunity to test our framework and investigate the impact of sub-pixel inhomogeneity on the MODIS τ and r_e retrievals. For this purpose, we selected a case shown in Figure 12. The granule in Figure 12a was collected by MODIS onboard the Terra satellite on September 9th 2006 over the Gulf of Mexico. We further selected a small region off the coast of Louisiana marked in the red box for our test. A zoom-in view of this small region at the 1km and 500m resolutions is shown in Figure 12b and Figure 12c, respectively.

Similar to the LES example, we first developed two sets of cloud property retrievals, one at a higher spatial resolution of 500 m and the other at a coarser resolution of 1 km. Figure 13a and b show the 500 m resolution τ and r_e retrievals, respectively, based on the combination of 0.86 and 2.1 µm reflectances for the selected region in Figure 12b. The 1 km retrievals are shown in Figure 13c and d. This scene has a cloud fraction of about 72%. In the center of the scene is a cluster of thick clouds with τ around 20 to 30, and r_e ranging mainly between 15µm to 20µm. Note that in our framework the 500 m retrievals are the sub-pixel $\tau\left(R_{VIS,i},R_{SWIR,i}\right)$ and $r_e\left(R_{VIS,i},R_{SWIR,i}\right)$. The 1 km retrievals are $\tau\left(\overline{R_{VIS}},\overline{R_{SWIR}}\right)$ and $r_e\left(\overline{R_{VIS}},\overline{R_{SWIR}}\right)$. To derive the $\Delta\tau$ and Δr_e from our mathematical framework in Eq. (8), we compute the sub-pixel reflectance variances and covariances for every 1-km cloudy pixel from the 2x2 500-m sub-pixel reflectance observations. The results are shown in Figure 14. Similar to the LES case, we find that the 0.86 and 2.1 µm cloud reflectances are generally positively correlated over the thin cloud regions. The correlation becomes weak (close to zero) over the thick cloud regions. These results indicate that when the cloud is thin, the variability in both 0.86 and 2.1 µm bands is controlled mainly by τ. The variability of 2.1 µm cloud reflectances becomes primarily sensitive to r_e only when the cloud becomes optically thick.

The difference between the 1 km retrievals and the mean of 500 m retrievals are the biases, $\Delta\tau$ and Δr_e, caused by the homogeneous pixel assumption. Figure 15a and b show $\Delta\tau$ and Δr_e, respectively, based on Eq. (3). We found that $\Delta\tau$ is mainly negative particularly in the regions with thick clouds, while Δr_e is mainly positive particularly in the transition regions from thick to thin clouds. These results are very similar to what we found in the LES scene in Figure 9. Both $\Delta\tau$ and Δr_e are shown in Figure 15c and d, respectively. The $\Delta\tau$ and Δr_e predicted from Eq. (8) agree reasonably well with the results derived from numerical retrievals in Figure 15a and b. The predicted $\Delta\tau$ based on Eq. (9) and the numerical results have a correlation coefficient over 0.85 for all cloudy pixels (over 0.95 for pixels with $\tau > 5$). The correlation coefficient for Δr_e is significantly lower especially for thin clouds with $\tau < 5$. This is mainly because when the cloud is thin the 2.1 µm cloud reflectances are not very sensitive to r_e. As a result, the retrievals are subject to large uncertainties caused by radiative transfer model uncertainties. If we limited the comparison only to clouds with $\tau > 5$, the correlation coefficient is over 0.70.

In summary, our numerical framework work very well for the LES cases, indicating that the high-order terms are mostly negligible in these cases. It also works reasonably well for the real MODIS case, especially for the clouds with $\tau > 5$. For thinner clouds, it is difficult to tell whether the deviation stems from higher-order terms or retrieval uncertainties. Another factor to consider is that we only have four 500 m sub-pixels for each 1 km pixel, which may be insufficient for deriving meaningful sub-pixel variance and co-variance. As part of ongoing research, we are trying to retrieve τ and r_e from the Advanced Space-borne Thermal Emission and Reflection Radiometer (ASTER) on Terra. ASTER has a much greater spatial resolution than MODIS and therefore can provide much richer information on small scale variability of cloud reflectance [*Zhao and Di Girolamo*, 2006; *Wen et al.*, 2007]. We will further test our framework using ASTER observations in future work.

5. Summary and Discussion

The impact of unresolved sub-pixel level variation of cloud reflectances is an important source of uncertainty in the bi-spectral solar reflective method. In this study, we develop a mathematical framework for understanding this impact and quantifying the consequent biases, $\Delta\tau$ and Δr_e. We show in Eq. (8) that $\Delta\tau$ and Δr_e are determined by two factors—the nonlinearity of the LUT and the inhomogeneity of reflectances within the pixel. We tested our framework using LES cloud fields and real MODIS observations. The results indicate that, in comparison with previous studies, our framework provides a more comprehensive explanation and also a more accurate estimation of the retrieval biases caused by the sub-pixel level variation of cloud reflectances. Most importantly, it demonstrates that sub-pixel variations in cloud reflectance can lead to both positive and negative values of Δr_e. In both the LES and MODIS cases that we examined, Δr_e were dominantly positive, hence contributing to the dominantly positive bias in retrieved r_e from resolved cloud variability.

Our framework could have several applications. For example, it can be used to understand the differences between retrievals made at different spatial resolutions (e.g., MODIS vs. SEVIRI) or based on different spectral reflectances (e.g., MODIS 2.1 µm vs. 3.7 µm). It could also useful for estimating retrieval uncertainties. For example, the retrieval uncertainty caused by sub-pixel reflectance variation in the operational 1 km

MODIS cloud products can be estimated based on our framework from the 500 m cloud reflectances. It can also be integrated into the operational MODIS retrieval algorithm to determine in real-time whether the high-resolution retrievals (e.g., from 1km to 500m) are necessary for a given pixel. Another useful application is to help the trade-off studies for instrument design. For example, the Ocean Color Imager (OCI) is the key instrument planned for NASA's coming Pre-Aerosol, Clouds, and ocean Ecosystem mission (http://decadal.gsfc.nasa.gov/pace.html). An important part of the OCI design trade-off study is to determine the optimal spatial resolution for both ocean color and atmospheric observations, including cloud property retrievals. Our framework would be highly useful for such study.

Finally, we feel necessary to clarify again that our framework cannot explain or predict 3-D effects, such as the illuminating, shadowing, and photon leaking, which are known to substantially influence cloud reflectances and therefore retrieval results. These effects are beyond the scope of this study. Our framework simply predicts the statistical differences between retrievals with different spatial resolutions, regardless of whether the radiative transfer is 1-D or 3-D.

Acknowledgement:

This research is supported by NASA grants NNX14AJ25G and NNX15AC77G. The computations in this study were performed at the UMBC High Performance Computing Facility (HPCF). The facility is supported by the U.S. National Science Foundation through the MRI program (grant nos. CNS-0821258 and CNS-1228778) and the SCREMS program (grant no. DMS-0821311), with additional substantial support from UMBC. The MODIS data are obtained from NASA's Level 1 and Atmosphere Archive and Distribution System (LAADS http://ladsweb.nascom.nasa.gov/).

References:

Ackerman, A. S., M. P. Kirkpatrick, D. E. Stevens, and O. B. Toon (2004), The impact of humidity above stratiform clouds on indirect aerosol climate forcing, ***Nature***, ***432***(7020), 1014–1017, doi:10.1038/nature03174.

Barker, H. W. (1996), A Parameterization for Computing Grid-Averaged Solar Fluxes for Inhomogeneous Marine Boundary Layer Clouds. Part I: Methodology and Homogeneous Biases, ***JAS***, ***53***(16), 2289–2303, doi:10.1175/1520-0469(1996)053<2289:APFCGA>2.0.CO;2.

Cahalan, R. F., and J. H. Joseph (1989), Fractal statistics of cloud fields, ***Monthly Weather Review***, ***117***(2), 261–272.

Cahalan, R. F., W. Ridgway, W. J. Wiscombe, T. L. Bell, and J. B. Snider (1994), The Albedo of Fractal Stratocumulus Clouds, ***J. Atmos. Sci.***, ***51***(16), 2434–2455, doi:10.1175/1520-0469(1994)051<2434:TAOFSC>2.0.CO;2.

Cho, H. M. et al. (2015), Frequency and causes of failed MODIS cloud property retrievals for liquid phase clouds over global oceans, ***Journal of Geophysical Research-Atmospheres***, ***120***(9), 2015JD023161–n/a, doi:10.1002/2015JD023161.

Davis, A., and A. Marshak (2010), 3D transport of solar radiation in clouds, ***Reports on Progress in Physics***.

Di Girolamo, L., L. Liang, and S. Platnick (2010), A global view of one-dimensional solar radiative transfer through oceanic water clouds, ***Geophys Res Lett***, ***37***(18), L18809.

Dong, X., T. P. Ackerman, E. E. Clothiaux, P. Pilewskie, and Y. Han (1997), Microphysical and radiative properties of boundary layer stratiform clouds deduced from ground-based measurements, ***J. Geophys. Res.***, ***102***(D20), 23829–23843, doi:10.1029/97JD02119.

Harshvardhan, and D. A. Randall (1985), Comments on “The Parameterization of Radiation for Numerical Weather Prediction and Climate Models,” ***Mon. Wea. Rev***, ***113***(10), 1832–1833, doi:10.1175/1520-0493(1985)113<1832:COPORF>2.0.CO;2.

Kato, S., L. M. Hinkelman, and A. Cheng (2006), Estimate of satellite-derived cloud optical thickness and effective radius errors and their effect on computed domain-averaged irradiances, ***J. Geophys. Res.***, ***111***(D17), D17201, doi:10.1029/2005JD006668.

Liang, L., and L. D. Girolamo (2013), A global analysis on the view-angle dependence of plane-parallel oceanic liquid water cloud optical thickness using data synergy from

MISR and MODIS, ***Journal of Geophysical Research-Atmospheres***, ***118***(5), 2389–2403, doi:10.1029/2012JD018201.

Liang, L., L. Di Girolamo, and S. Platnick (2009), View-angle consistency in reflectance, optical thickness and spherical albedo of marine water-clouds over the northeastern Pacific through MISR-MODIS fusion, ***Geophysical Research Letters***, ***36***(9), L09811, doi:10.1029/2008GL037124.

Liang, L., L. Di Girolamo, and W. Sun (2015), Bias in MODIS cloud drop effective radius for oceanic water clouds as deduced from optical thickness variability across scattering angles, ***Journal of Geophysical Research-Atmospheres***, ***120***(15), 7661–7681, doi:10.1002/2015JD023256.

Marshak, A., S. Platnick, T. Várnai, G. Wen, and R. F. Cahalan (2006), Impact of three-dimensional radiative effects on satellite retrievals of cloud droplet sizes, ***J. Geophys. Res.***, ***111***(D9), D09207, doi:10.1029/2005JD006686.

Minnis, P. et al. (2011), CERES Edition-2 Cloud Property Retrievals Using TRMM VIRS and Terra and Aqua MODIS Data-Part I: Algorithms, ***IEEE TRANSACTIONS ON GEOSCIENCE AND REMOTE SENSING***, ***49***(11), 4374–4400, doi:10.1109/TGRS.2011.2144601.

Nakajima, T., and M. D. King (1990), Determination of the Optical Thickness and Effective Particle Radius of Clouds from Reflected Solar Radiation Measurements. Part I: Theory, ***J. Atmos. Sci.***, ***47***(15), 1878–1893, doi:10.1175/1520-0469(1990)047<1878:DOTOTA>2.0.CO;2.

Oreopoulos, L., and R. Davies (1998), Plane Parallel Albedo Biases from Satellite Observations. Part I: Dependence on Resolution and Other Factors, ***Journal of Climate***, ***11***(5), 919–932.

Oreopoulos, L., R. F. Cahalan, and S. Platnick (2007), The Plane-Parallel Albedo Bias of Liquid Clouds from MODIS Observations, ***Journal of Climate***, ***20***(20), 5114–5125, doi:10.1175/JCLI4305.1.

Painemal, D., and P. Zuidema (2011), Assessment of MODIS cloud effective radius and optical thickness retrievals over the Southeast Pacific with VOCALS-REx in situ measurements, ***J Geophys Res***, ***116***(D24), D24206.

Pincus, R., and K. F. Evans (2009), Computational Cost and Accuracy in Calculating Three-Dimensional Radiative Transfer: Results for New Implementations of Monte Carlo and SHDOM,, ***66***(10), 3131–3146, doi:10.1175/2009JAS3137.1.

Pincus, R., S. A. McFarlane, and S. A. Klein (1999), Albedo bias and the horizontal variability of clouds in subtropical marine boundary layers: Observations from ships and satellites, ***J. Geophys. Res.***, ***104***(D6), 6183–6191, doi:10.1029/1998JD200125.

Platnick, S., M. D. King, S. A. Ackerman, W. P. Menzel, B. A. Baum, J. C. Riédi, and R. A. Frey (2003), The MODIS cloud products: algorithms and examples from Terra, ***IEEE TRANSACTIONS ON GEOSCIENCE AND REMOTE SENSING***, ***41***(2), 459–473, doi:10.1109/TGRS.2002.808301.

Roebeling, R., A. Feijt, and P. Stammes (2006), Cloud property retrievals for climate monitoring: Implications of differences between Spinning Enhanced Visible and Infrared Imager (SEVIRI) on METEOSAT-8 and Advanced Very High Resolution Radiometer (AVHRR) on NOAA-17, ***J Geophys Res***, ***111***, D20210.

Stamnes, K., S. Tsay, K. Jayaweera, and W. Wiscombe (1988), Numerically stable algorithm for discrete-ordinate-method radiative transfer in multiple scattering and emitting layered media,, ***27***(12), 2502–2509.

Stevens, D. E., A. S. Ackerman, and C. S. Bretherton (2010), Effects of Domain Size and Numerical Resolution on the Simulation of Shallow Cumulus Convection, ***http://dx.doi.org/10.1175/1520-0469(2002)059<3285:EODSAN>2.0.CO;2***, ***59***(23), 3285–3301, doi:10.1175/1520-0469(2002)059<3285:EODSAN>2.0.CO;2.

Várnai, T., and A. Marshak (2002), Observations of Three-Dimensional Radiative Effects that Influence MODIS Cloud Optical Thickness Retrievals, ***J. Atmos. Sci.***, ***59***(9), 1607–1618, doi:10.1175/1520-0469(2002)059<1607:OOTDRE>2.0.CO;2.

Walther, A., and A. K. Heidinger (2012), Implementation of the Daytime Cloud Optical and Microphysical Properties Algorithm (DCOMP) in PATMOS-x, ***J. Appl. Meteor. Climatol.***, ***51***(7), 1371–1390, doi:10.1175/JAMC-D-11-0108.1.

Wen, G., A. Marshak, R. F. Cahalan, L. A. Remer, and R. G. Kleidman (2007), 3-D aerosol-cloud radiative interaction observed in collocated MODIS and ASTER images of cumulus cloud fields, ***J. Geophys. Res.***, ***112***(D13).

Zhang, Z. (2013), On the sensitivity of cloud effective radius retrieval based on spectral method to bi-modal droplet size distribution: A semi-analytical model, ***Journal of Quantitative Spectroscopy and Radiative Transfer VL -***, (0 SP - EP - PY - T2 -), doi:10.1016/j.jqsrt.2013.05.033.

Zhang, Z., A. S. Ackerman, G. Feingold, S. Platnick, R. Pincus, and H. Xue (2012), Effects of cloud horizontal inhomogeneity and drizzle on remote sensing of cloud droplet effective radius: Case studies based on large-eddy simulations, ***J Geophys Res***, ***117***(D19), D19208–, doi:10.1029/2012JD017655.

Zhang, Z., and S. Platnick (2011), An assessment of differences between cloud effective particle radius retrievals for marine water clouds from three MODIS spectral bands, ***J Geophys Res***, ***116***(D20), D20215, doi:10.1029/2011JD016216.

Zhao, G., and L. Di Girolamo (2006), Cloud fraction errors for trade wind cumuli from EOS-Terra instruments, ***Geophysical Research Letters***, ***33***(20), L20802, doi:10.1029/2006GL027088.

Figures

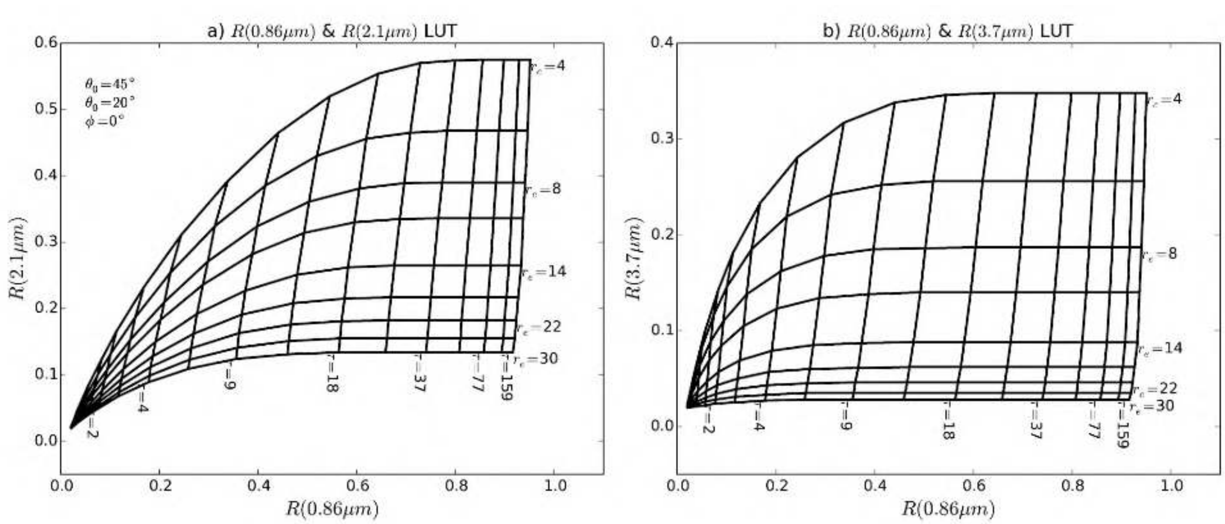

Figure 1 Examples of the look-up table of cloud bi-directional reflection function as functions of cloud optical thickness and effective radius, based on the combination of a) 0.86 and 2.1 µm bands, and b) 0.86 and 3.7 µm bands. Surface is assumed to be Lambertian with a reflectance of 0.02. Solar and viewing zenith angle are 45° and 20°, respectively. Relative azimuthal angle is 0°.

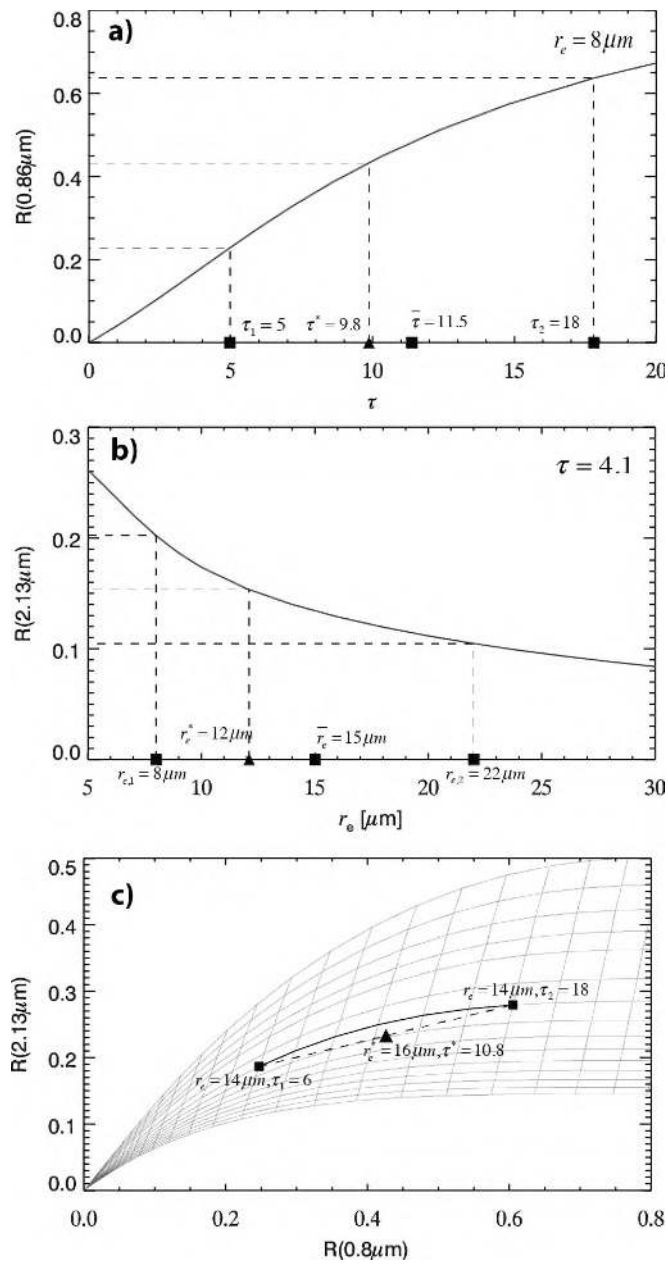

Figure 2 a) an example to illustrate the PPHB bias proposed in Cahalan et al. [1994] for τ retrieval, b) example to illustrate the PPHB bias proposed in Marshak et al. [2006], c) example to illustrate the r_e retrieval bias caused by sub-pixel τ variability proposed in Zhang and Platnick [2011] and Zhang et al. [2012]. See text for details. Solar and view zenith angles are assume to be 20° and 0° and relative azimuth angle is assumed to be 30° in these cases.

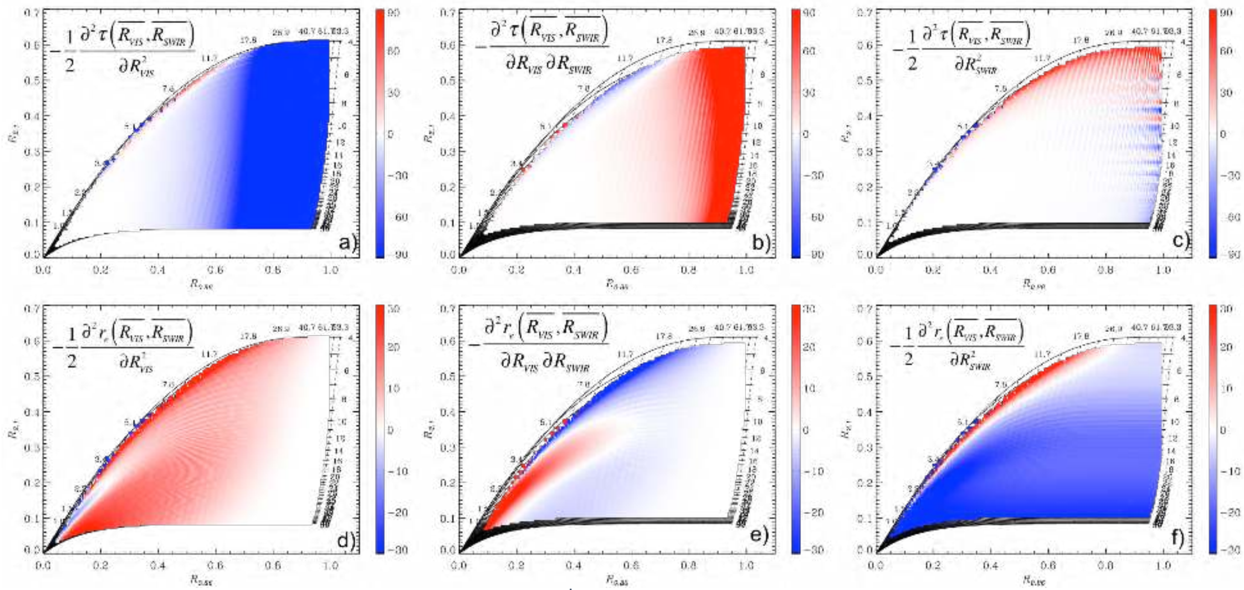

Figure 3 The sign and magnitude of each 2[nd] derivative term in Eq. *(8)* derived from the $R_{0.86}$ and R2.1 LUT. a) corresponds to $-\frac{1}{2}\frac{\partial^2 \tau\left(\overline{R_{VIS}},\overline{R_{SWIR}}\right)}{\partial R_{VIS}^2}$*, b) to* $-\frac{\partial^2 \tau\left(\overline{R_{VIS}},\overline{R_{SWIR}}\right)}{\partial R_{VIS}\,\partial R_{SWIR}}$*, c) to* $-\frac{1}{2}\frac{\partial^2 \tau\left(\overline{R_{VIS}},\overline{R_{SWIR}}\right)}{\partial R_{SWIR}^2}$*, d) to* $-\frac{1}{2}\frac{\partial^2 r_e\left(\overline{R_{VIS}},\overline{R_{SWIR}}\right)}{\partial R_{VIS}^2}$*, e) to* $-\frac{\partial^2 r_e\left(\overline{R_{VIS}},\overline{R_{SWIR}}\right)}{\partial R_{VIS}\,\partial R_{SWIR}}$*, and f) to* $-\frac{1}{2}\frac{\partial^2 r_e\left(\overline{R_{VIS}},\overline{R_{SWIR}}\right)}{\partial R_{SWIR}^2}$*.* Solar and view zenith angles are assumed to be 20° and 0°, relative azimuth angle is assumed to be 30° in these cases.

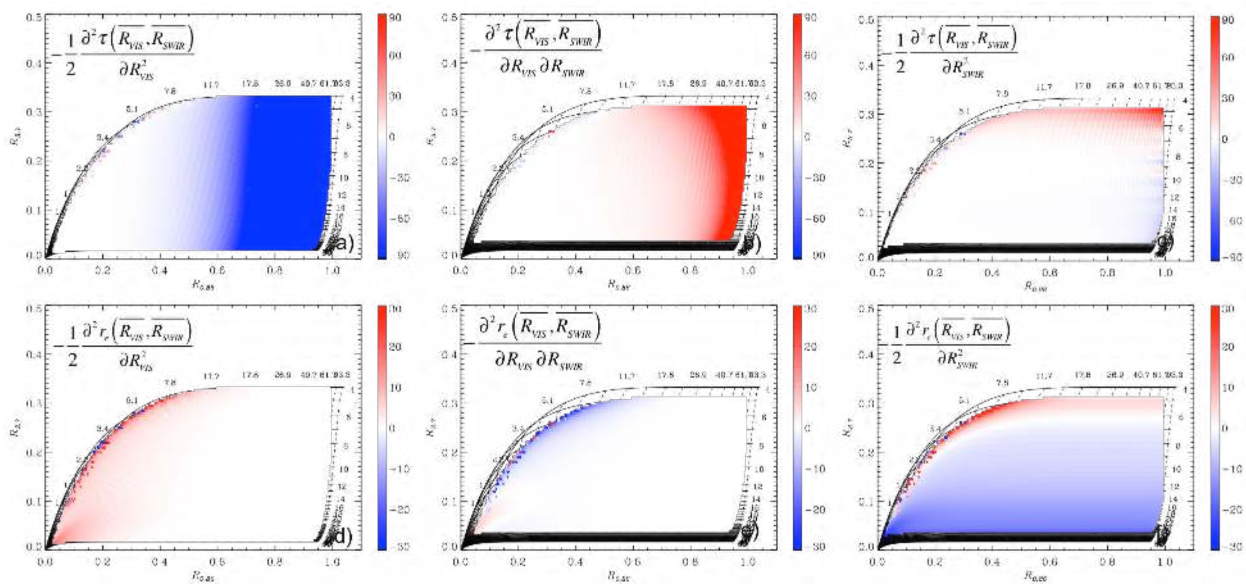

Figure 4 Same as Figure 3 , except for the $R_{0.86}$ and $R_{3.7}$ LUT. Solar and view zenith angles are assume to be 20° and 0° and relative azimuth angle is assumed to be 30° in these cases.

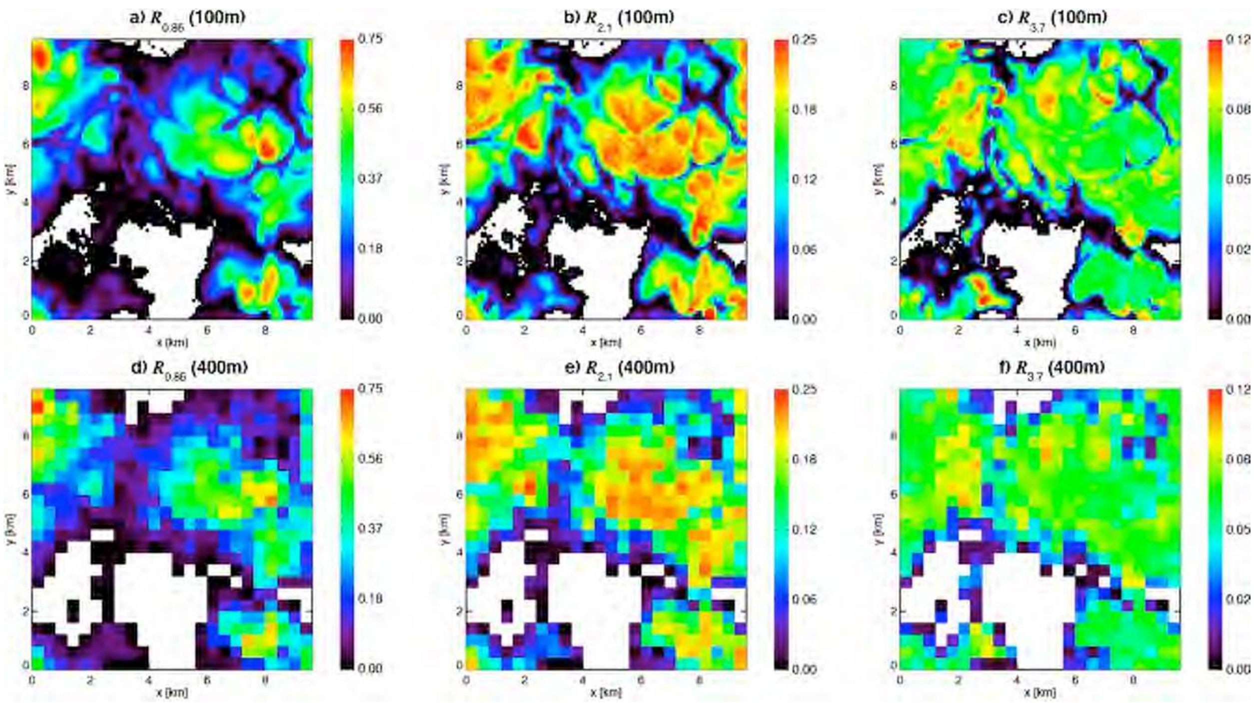

Figure 5 Simulated a) 0.86 µm, b) 2.1 µm and c) 3.7 µm MODIS bi-directional reflectances at 100-m resolution for the LES cloud field. d)—f) 400-m bi-directional reflectances averaged from 100-m resolution simulations.

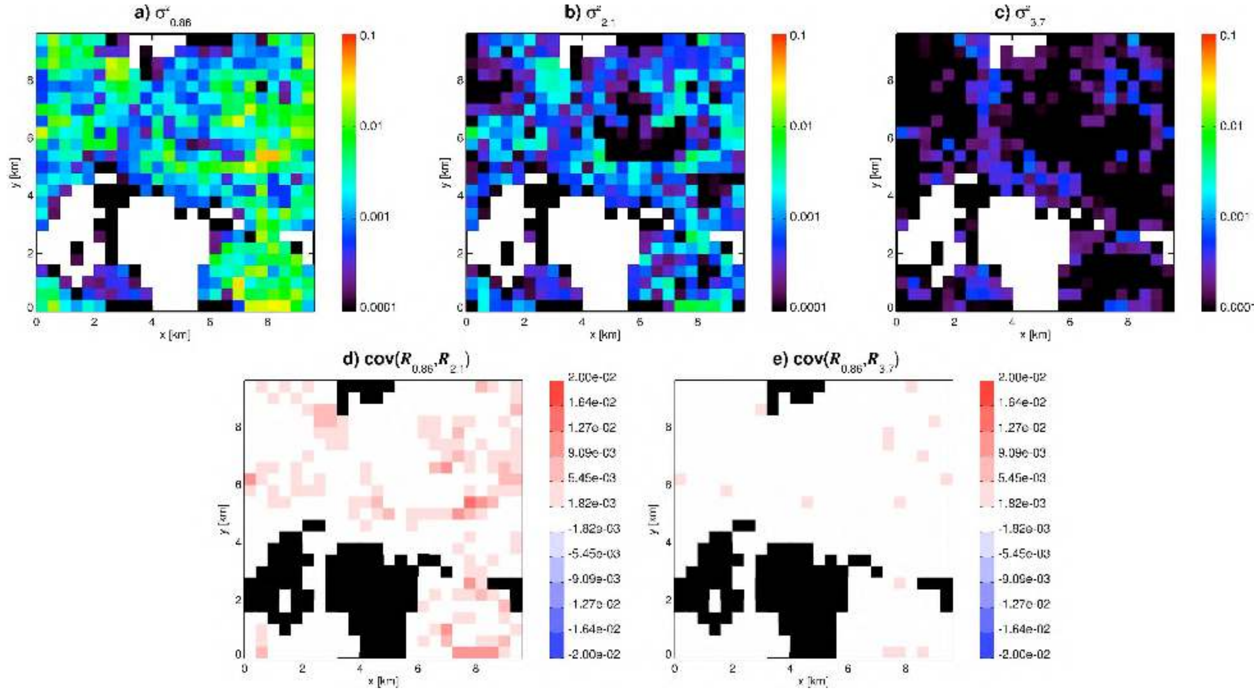

Figure 6 The sub-pixel reflectance variance a) $\sigma_{0.86}^2$, b) $\sigma_{2.1}^2$, c) $\sigma_{3.7}^2$ and covariances d) $\mathrm{cov}(R_{0.86}, R_{2.1})$ and e) $\mathrm{cov}(R_{0.86}, R_{3.7})$ for the LES case in Figure 5.

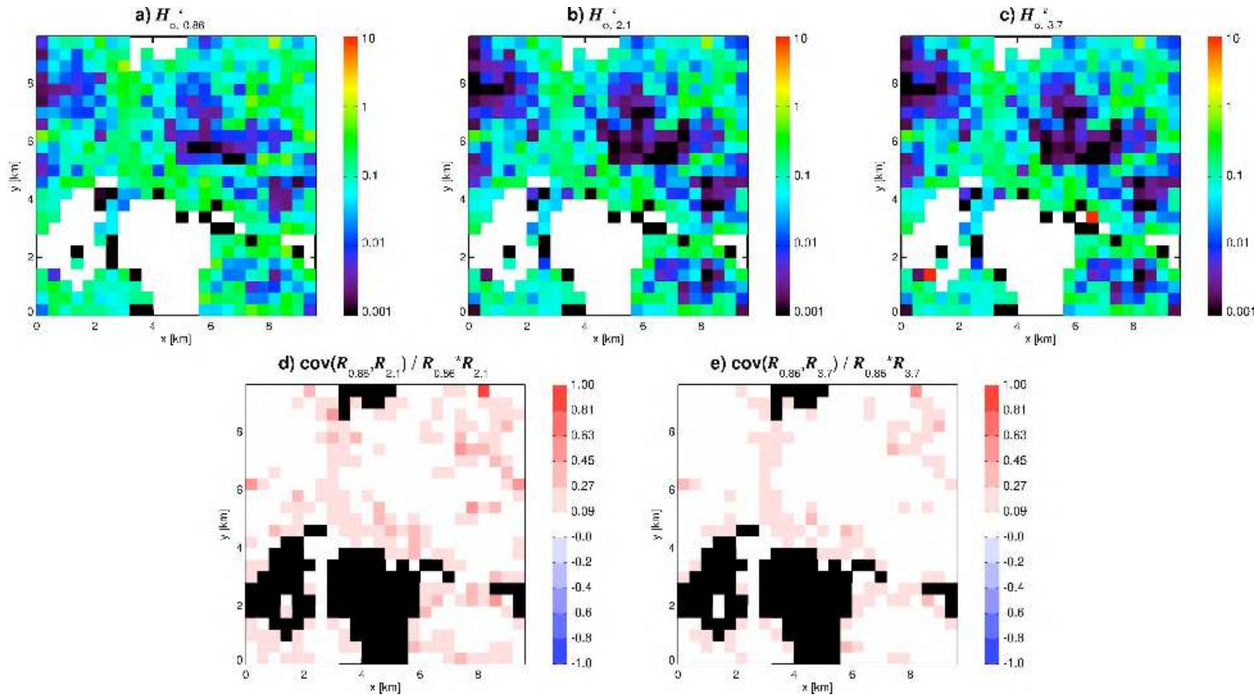

Figure 7 The sub-pixel a) $H^2_{\sigma_{0.86}}$, b) $H^2_{\sigma_{2.1}}$, c) $H^2_{\sigma_{3.7}}$ d) $\mathrm{cov}\left(R_{0.86}, R_{2.1}\right) / \left(\overline{R_{0.86}}, \cdot \overline{R_{2.1}}\right)$ and e) $\mathrm{cov}\left(R_{0.86}, R_{3.7}\right) / \left(\overline{R_{0.86}}, \cdot \overline{R_{3.7}}\right)$ for the LES case in Figure 5.

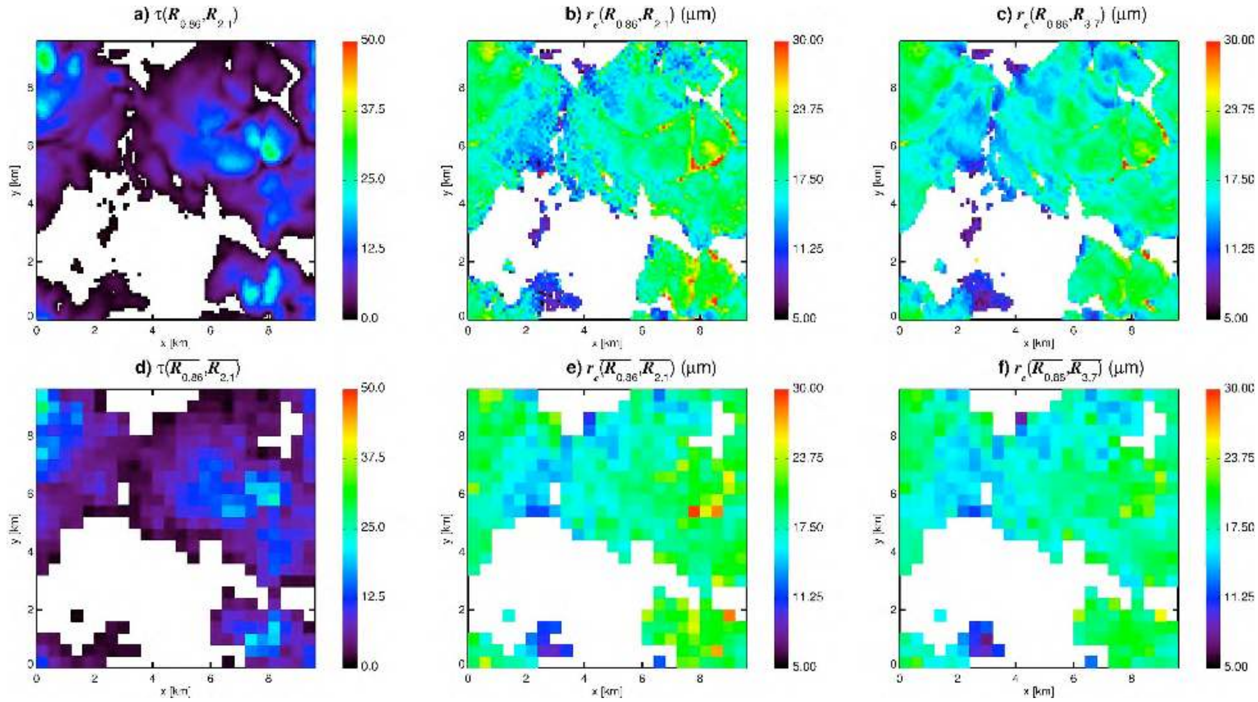

Figure 8 a) τ , b) $r_{e,2.1}$ and c) $r_{e,3.7}$ retrievals based on the 100 m reflectance. d)—f) retrievals based on the 400 m reflectance.

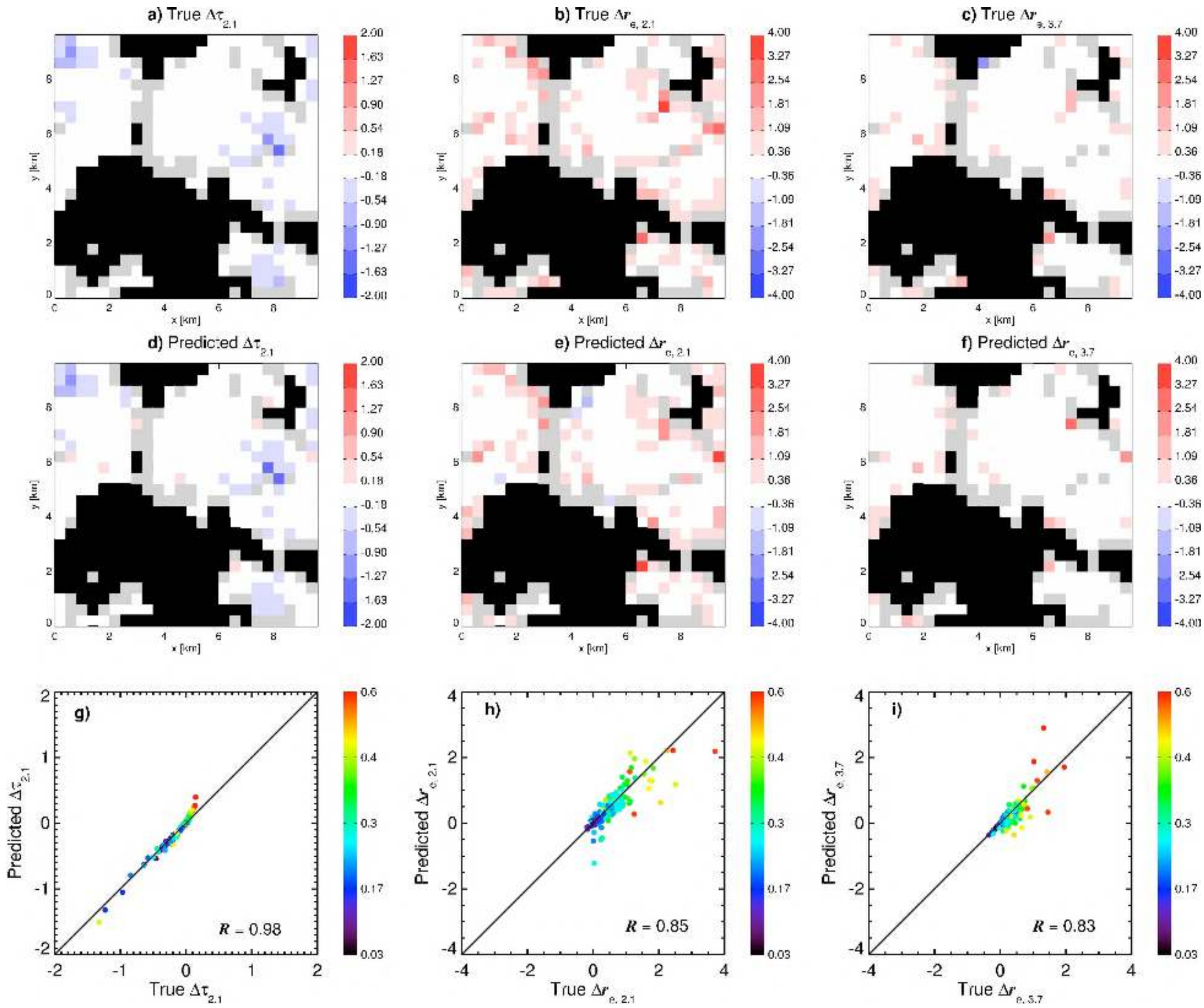

Figure 9 The a) $\Delta\tau$, b) $\Delta r_{e,2.1}$ and c) $\Delta r_{e,3.7}$ derived based on the Eq. (3). The corresponding results obtained based on Eq. (8) are shown in d)—f). The pixel-to-pixel comparisons are shown in g)—i), in which the color indicate the value of the sub-pixel inhomogeneity index $H_{\sigma_{0.86}}$.

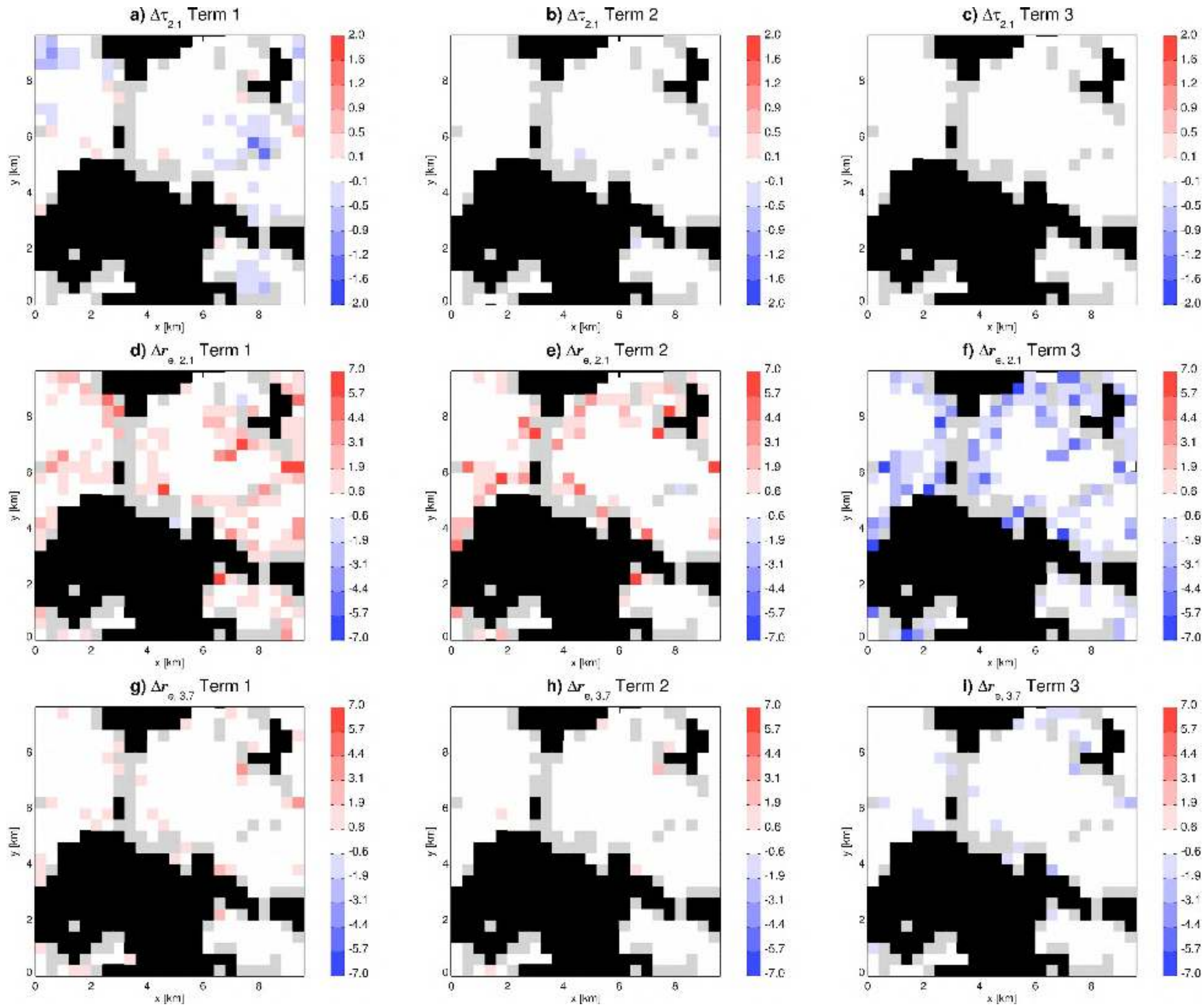

Figure 10 The decomposition of $\Delta\tau$ and Δr_e into the contributions from each term in the matrix of 2nd derivative. **a)** contribution of $-\frac{1}{2}\frac{\partial^2\tau\left(\overline{R_{0.86}},\overline{R_{2.1}}\right)}{\partial R_{0.86}^2}\cdot\sigma_{0.86}^2$ to $\Delta\tau$, **b)** contribution of $-\frac{1}{2}\frac{\partial^2\tau\left(\overline{R_{0.86}},\overline{R_{2.1}}\right)}{\partial R_{0.86}\,\partial R_{2.1}}\cdot\mathrm{cov}\left(R_{0.86},R_{2.1}\right)$ to $\Delta\tau$, **c)** contribution of $-\frac{1}{2}\frac{\partial^2\tau\left(\overline{R_{0.86}},\overline{R_{2.1}}\right)}{\partial R_{2.1}^2}\cdot\sigma_{2.1}^2$ to $\Delta\tau$. **d)** contribution of $-\frac{1}{2}\frac{\partial^2 r_e\left(\overline{R_{0.86}},\overline{R_{2.1}}\right)}{\partial R_{0.86}^2}\cdot\sigma_{0.86}^2$ to $\Delta r_{e,2.1}$, **e)** contribution of $-\frac{1}{2}\frac{\partial^2 r_e\left(\overline{R_{0.86}},\overline{R_{2.1}}\right)}{\partial R_{0.86}\,\partial R_{2.1}}\cdot\mathrm{cov}\left(R_{0.86},R_{2.1}\right)$ to $\Delta r_{e,2.1}$, **f)** contribution of $-\frac{1}{2}\frac{\partial^2 r_e\left(\overline{R_{0.86}},\overline{R_{2.1}}\right)}{\partial R_{2.1}^2}\cdot\sigma_{2.1}^2$ to $\Delta r_{e,2.1}$. **g)**

contribution of $-\frac{1}{2}\frac{\partial^2 \tau\left(\overline{R_{0.86}},\overline{R_{3.7}}\right)}{\partial R_{3.7}^2}\cdot\sigma_{3.7}^2$ to $\Delta r_{e,3.7}$. **h)** contribution of $-\frac{1}{2}\frac{\partial^2 r_e\left(\overline{R_{0.86}},\overline{R_{3.7}}\right)}{\partial R_{0.86}\,\partial R_{3.7}}\cdot\mathrm{cov}\left(R_{0.86},R_{3.7}\right)$ to $\Delta r_{e,3.7}$, **f)** contribution of $-\frac{1}{2}\frac{\partial^2 r_e\left(\overline{R_{0.86}},\overline{R_{3.7}}\right)}{\partial R_{3.7}^2}\cdot\sigma_{3.7}^2$ to $\Delta r_{e,2.1}$.

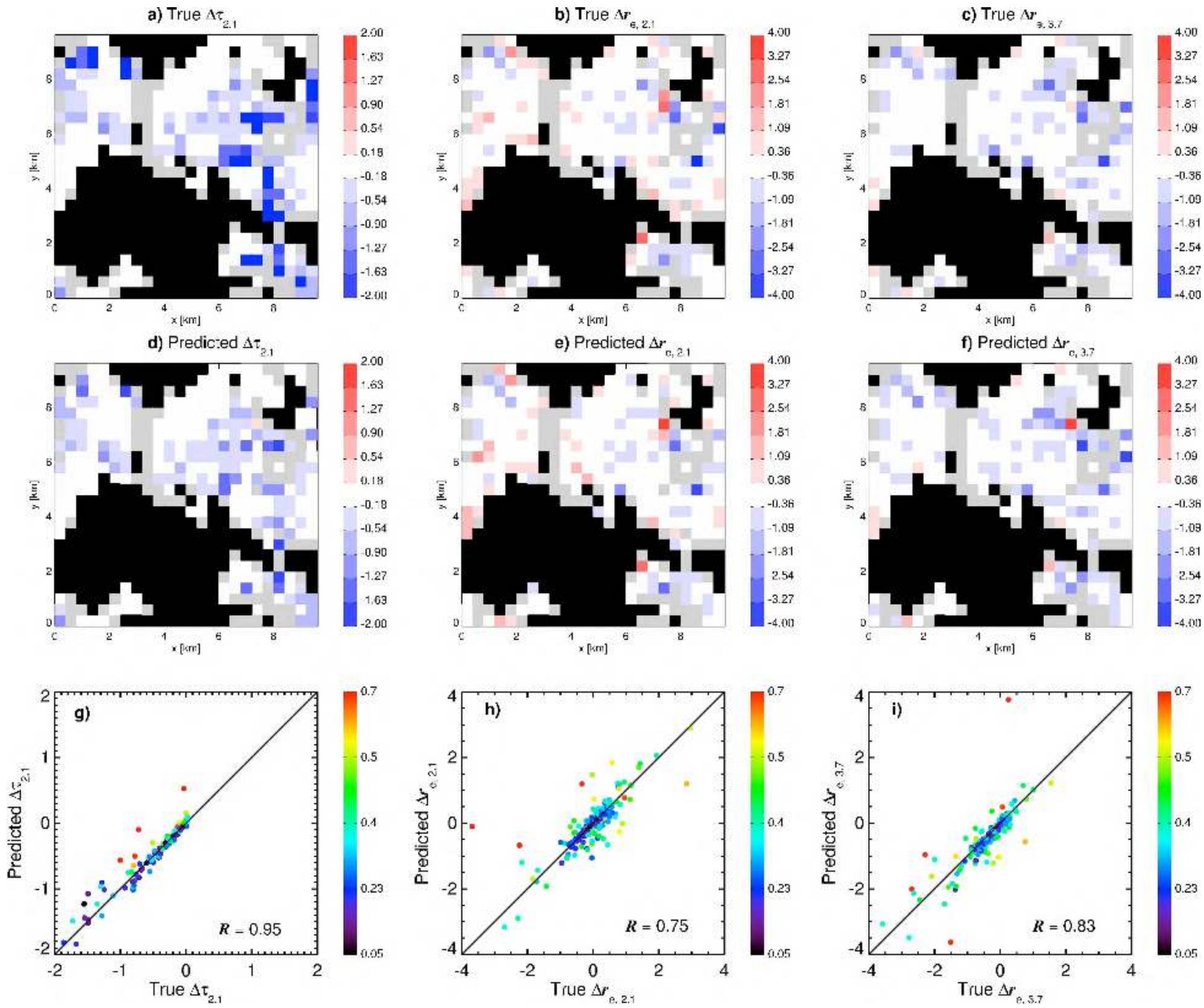

Figure 11 Same as Figure 9, except that in this case the solar zenith angle is 60°.

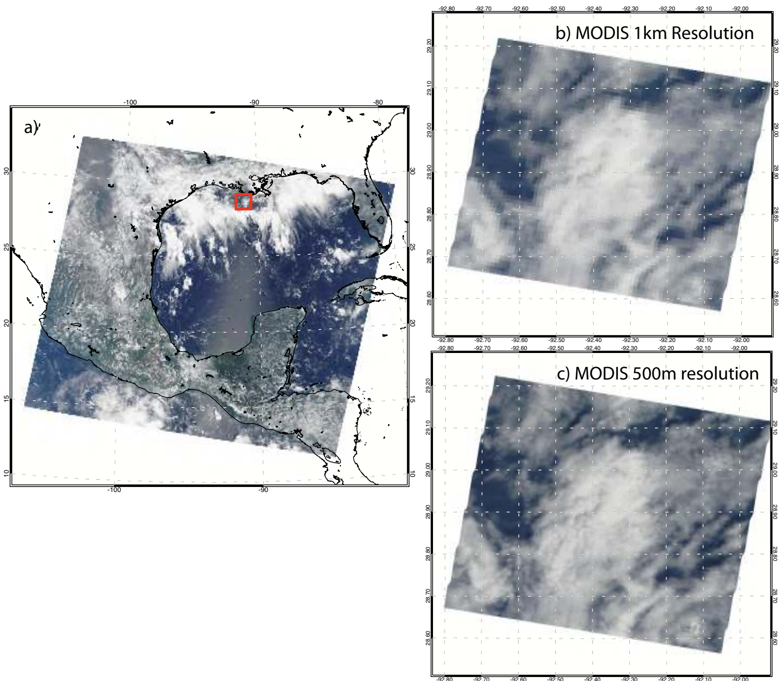

Figure 12 The a) RGB image of a MODIS granule collected on September 9th 2006 over the Gulf of Mexico. A zoom-in view of the region in the red box based on b) 1 km MODIS true color RGB image and c) 500 m MODIS true color RGB image..

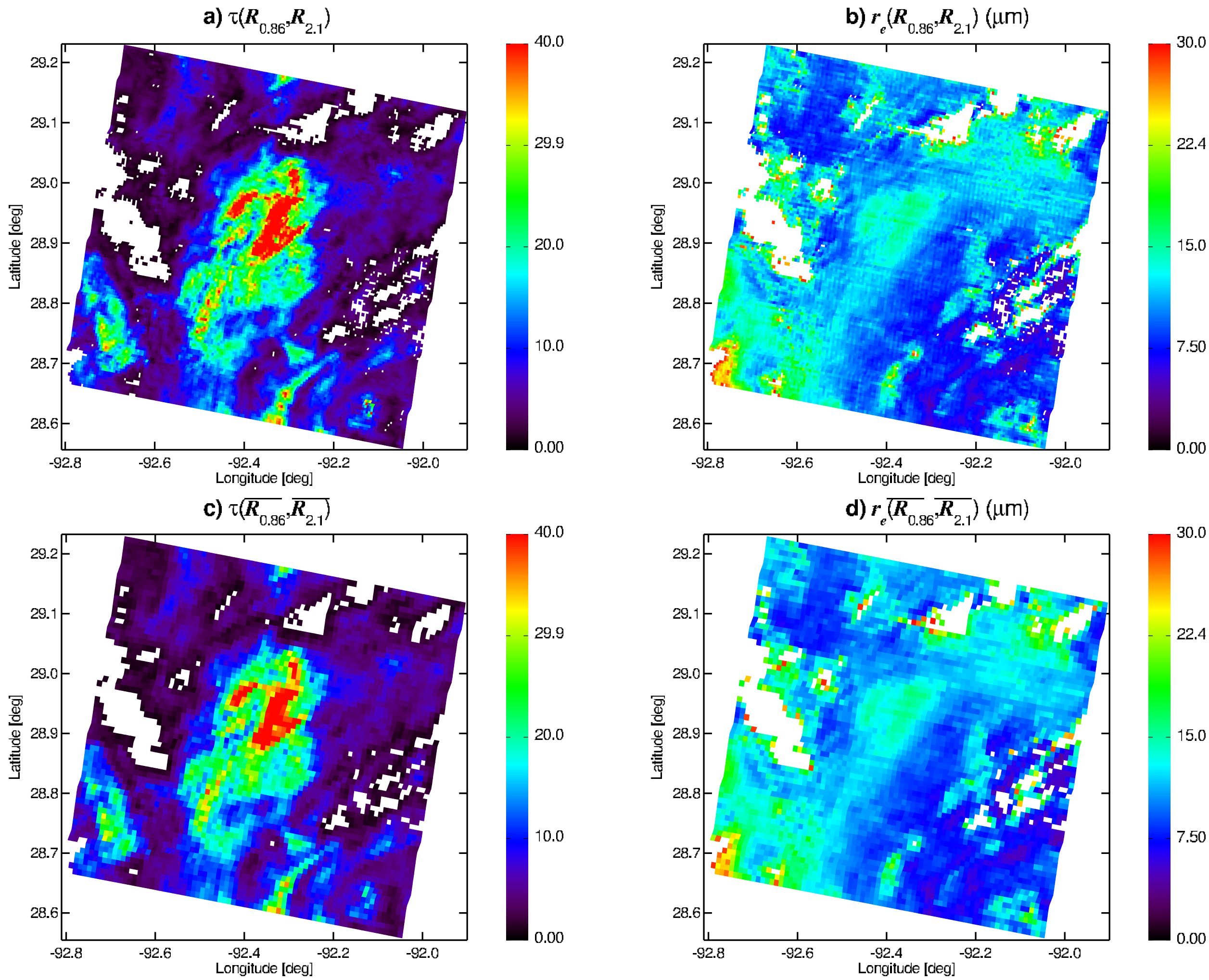

Figure 13 τ and $r_{e,2.1}$ retrievals for the region in Figure 12b at the 500 m (a) and b)) and 1 km (c) and d)) resolutions. The differences between 1km retrievals and the aggregated 500m retrievals , i.e., $\Delta\tau$ and $\Delta r_{e,2.1}$, are shown in e) and f).

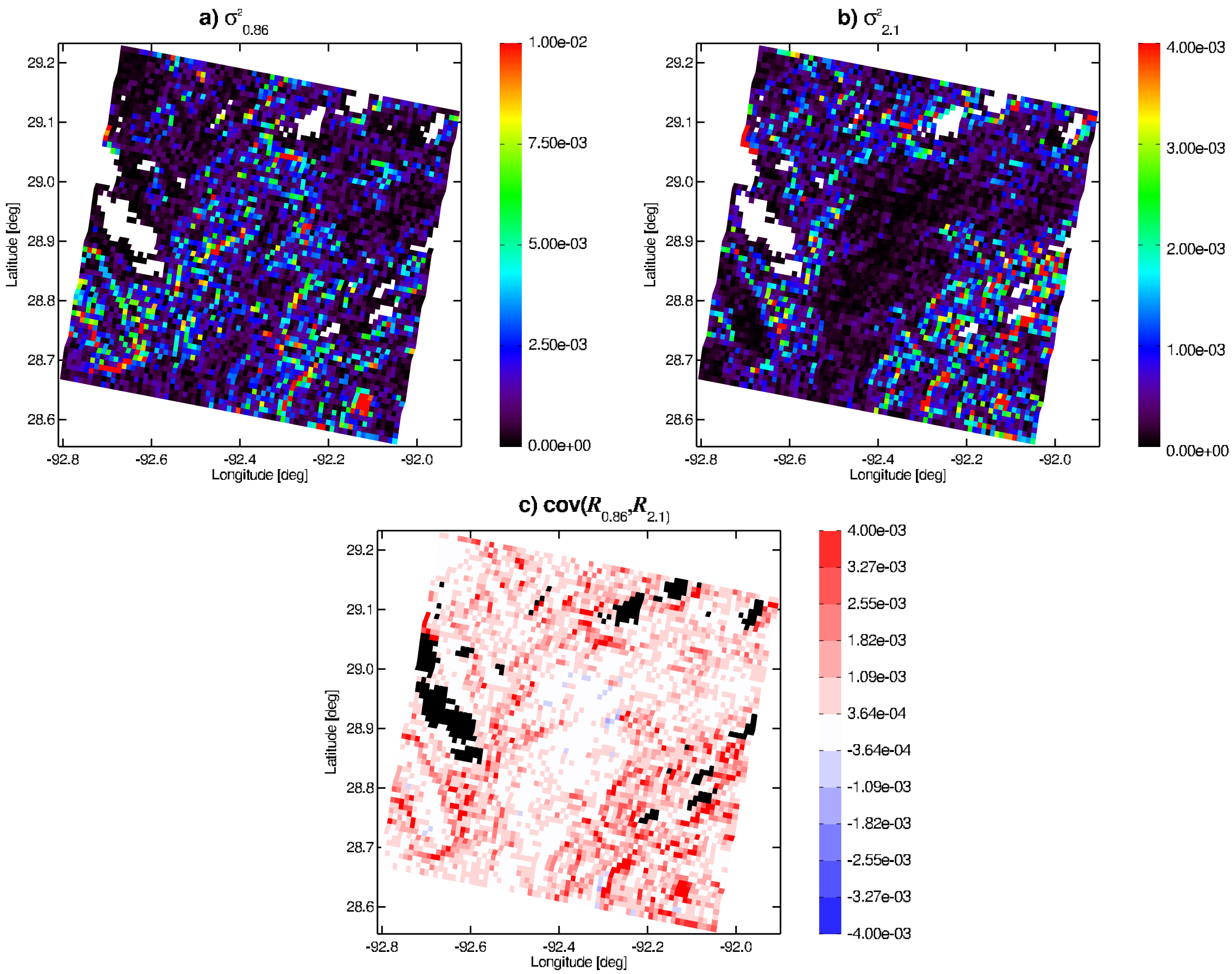

Figure 14 The sub-pixel reflectance variances a) $\sigma^2_{0.86}$, b) $\sigma^2_{2.1}$, and covariances c) $\mathrm{cov}\left(R_{0.86}, R_{2.1}\right)$ for the MODIS case in Figure 12b.

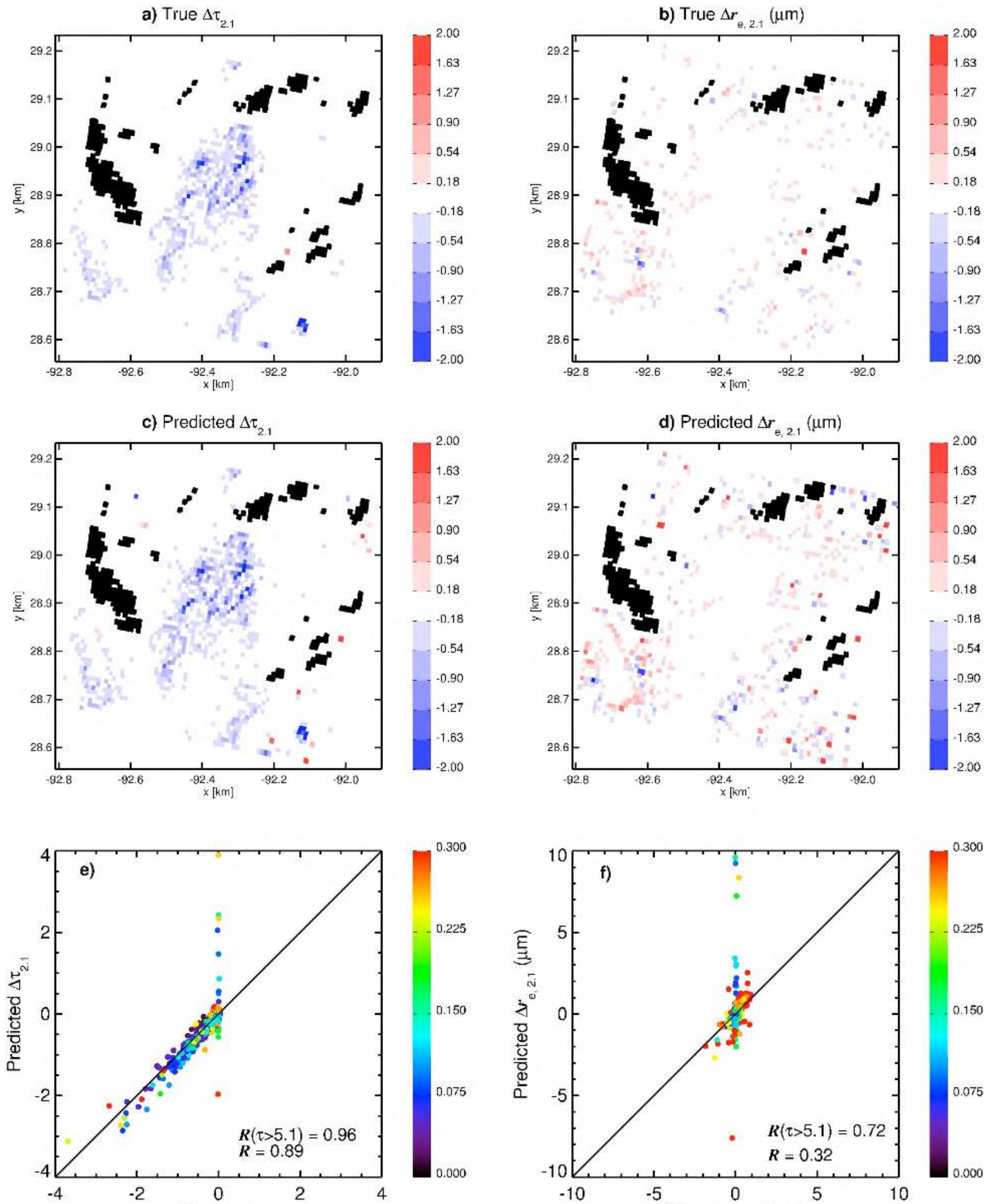

Figure 15 The a) $\Delta\tau$ and b) Δr_e derived based on the Eq. (3). The corresponding results based on Eq. (8) are shown in c) and d) and comparisons in e) and f).